

Multifidelity Data Fusion with Application to Blended-Wing-Body Multidisciplinary Analysis Under Uncertainty

Alex Feldstein *

Aurora Flight Sciences, Cambridge, MA, 02142, USA

David Lazzara † and Norman Princen ‡

The Boeing Company, Huntington Beach, CA, 92647, USA

Karen Willcox §

The University of Texas at Austin, Austin, TX, 78712, USA

This paper presents a methodology to support improved decision-making and identification of risks in early-stage multidisciplinary design. The approach fuses multifidelity data from disparate information sources available to designers, such as disciplinary simulations, experiments, and operational data from previously deployed systems. The multifidelity data fusion is achieved using a fidelity-weighted combination of Gaussian process surrogate models. This weighting takes into account both the quality of the Gaussian process approximation and the designer’s confidence in the underlying information source being approximated. The resulting multifidelity surrogate provides a rapid analysis capability, which in turn enables the high number of evaluations needed to conduct multidisciplinary trade studies and to propagate uncertainty to the overall system level. The methodology is broadly applicable across engineering design problems where multiple information sources are available to support design decisions. In this paper, the approach is demonstrated on the stability and control analysis of a Blended-Wing-Body aircraft’s center of gravity limits, considering the longitudinal criteria of fly-to-stall, stall recovery, nose-wheel steering, and nose-wheel liftoff. The results show that low-fidelity models are enhanced by the presence of higher-fidelity data in key areas of the design space. The presence of even sparse high-fidelity data is key to reducing the variance in the overall analysis, thereby improving the quality of the predictions needed to inform early-stage design decisions.

*Conceptual Design Engineer, feldstein.alex@aurora.aero, Member AIAA

†Aerodynamics Engineer, Member AIAA

‡Blended Wing Body Chief Engineer, Senior Member AIAA

§Director, Oden Institute for Computational Engineering and Sciences, kwillcox@oden.utexas.edu, Fellow AIAA

Nomenclature

C_L	=	Lift coefficient
C_D	=	Drag coefficient
$C_{m_{ref}}$	=	Pitching moment coefficient about the aerodynamic reference point
$C_{m_{CG}}$	=	Pitching moment coefficient about the center of gravity
\mathcal{D}	=	Quantity of interest input space
F_X, F_Z	=	Force in the body X/Z axis
\mathcal{GP}	=	Gaussian process
IB, OB	=	Inboard/Outboard control surface
I_{yy}	=	Moment of inertia about the Y axis
M	=	Mach number
M_Y	=	Moment about the body Y axis
\dot{Q}	=	Pitch acceleration
\mathbb{R}	=	Real numbers
$R_{mg/ng}$	=	Reaction force due to main/nose gear
S_{ref}	=	Reference area
\dot{U}, \dot{W}	=	Vehicle acceleration along the X/Z axis
V_∞	=	Freestream velocity
X	=	Matrix of training data
$\Delta X_{\square}, \Delta Z_{\square}$	=	Distance between the center of gravity and the \square gear along the X/Z axis
c_{ref}	=	Reference chord
d	=	Number of dimensions in input space
$f(x)$	=	quantity of interest
\tilde{f}	=	Surrogate model of quantity of interest
g	=	Acceleration due to gravity
$k(x, x)$	=	Gaussian Process kernel function
ℓ_k	=	Characteristic length of dimension k
m	=	Vehicle mass
$m(x)$	=	Gaussian Process mean function
n_δ	=	Number of control surfaces
\bar{q}	=	Dynamic pressure
\mathbf{x}_{aero}	=	Aerodynamic state vector
α	=	Angle of attack
δ_i	=	Deflection of control surface i
θ	=	Body angle with respect to the ground
μ	=	Coefficient of rolling friction
μ_{GP}	=	Mean of Gaussian Process
$\bar{\mu}$	=	Multifidelity mean estimate
σ	=	Covariance function scaling hyperparameter
σ_{GP}^2	=	Variance of Gaussian Process posterior estimate
σ_f^2	=	Fidelity variance
σ_t^2	=	Total variance
$\bar{\sigma}^2$	=	Multifidelity variance estimate

I. Introduction

Early-stage design decisions draw on multiple sources of information, including low- and high-fidelity disciplinary models, small-scale experiments, historical data, and expert opinion. It is a significant challenge to optimally exploit this range of multi-information-source data, requiring the designer to manage and control uncertainty while ensuring an appropriate level of fidelity to inform the design decision at hand. This challenge is amplified in the multidisciplinary setting, where nonlinear interactions among disciplines may cause uncertainty to manifest in unexpected ways at the system level. This is true for many aerospace systems, including aircraft, spacecraft, satellites, and more. This paper develops a methodology that fuses data from disparate information sources, quantifies the uncertainty in the fused

multi-information-source estimates, and propagates that uncertainty to the system level. As an illustrative example, we consider the stability and control (S&C) analysis of a Blended-Wing-Body (BWB) aircraft. This is a prime example where: (1) nonlinear multidisciplinary interactions drive critical early-stage design decisions; (2) evaluating critical design criteria requires many thousands of aerodynamic evaluations, rendering the use of high-fidelity models alone computationally prohibitive; (3) critical design criteria involve operating conditions outside the regimes of validity for typical low-fidelity aerodynamic conceptual design models; and (4) a combination of experimental data and simulation-based models are typically available to inform design decisions. The key elements of our approach are shown in Figure 1.

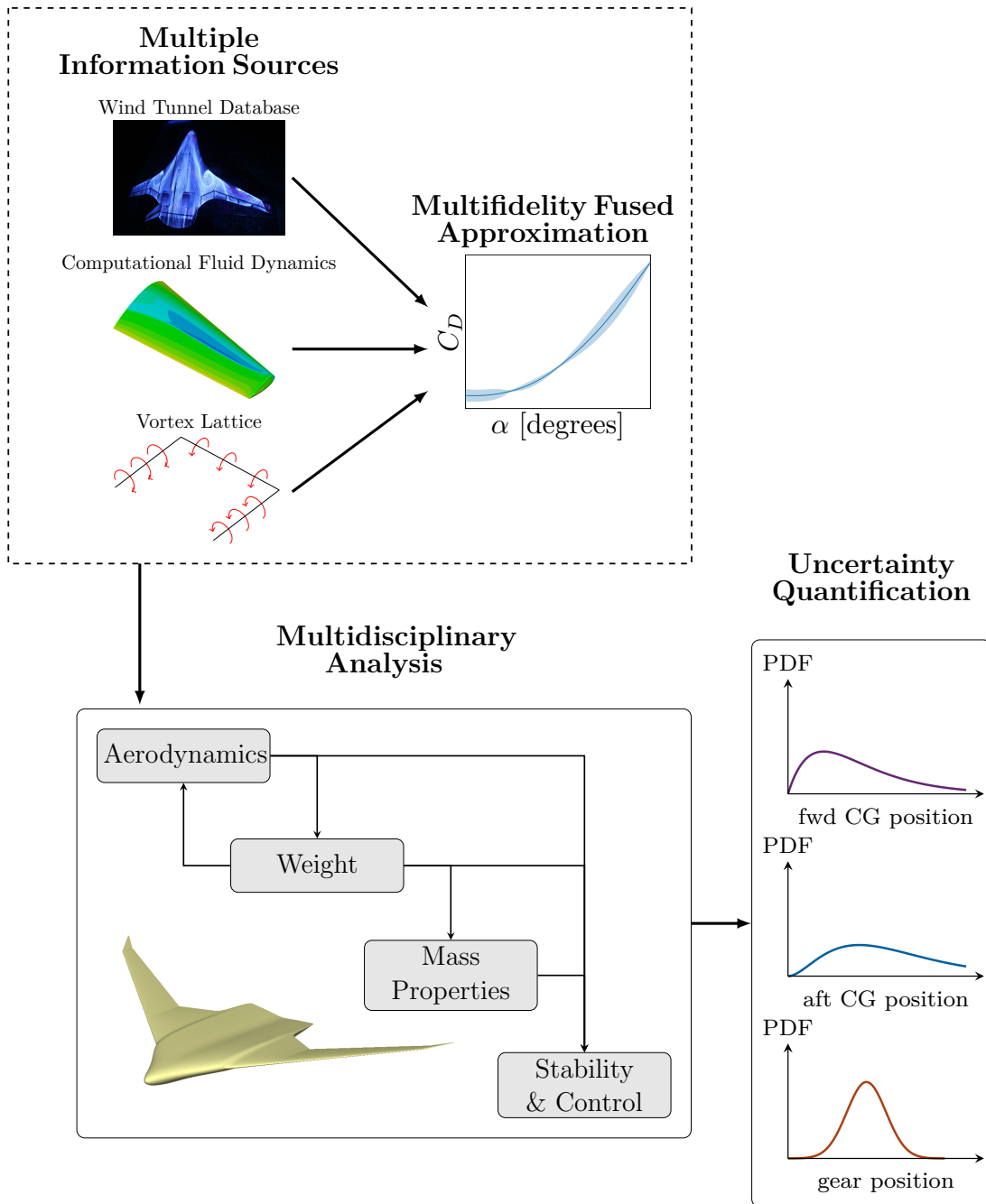


Fig. 1 Our multifidelity methodology combines multiple information sources and quantifies uncertainty at the integrated system level.

The BWB aircraft configuration is envisioned to serve the long-haul cargo transport market [1]. A key design driver of BWB configurations is the S&C analysis, which assesses control effectiveness and computes the operating center of gravity limits. Due to the tight coupling among aerodynamics, planform layout, and S&C in a BWB configuration, it is essential that the S&C constraints be considered early in the conceptual design process. The S&C analysis relies on accurate estimates of the aircraft’s lift, drag, and pitching moment coefficients [2]. Prior studies of BWB control surface layouts and controller designs have used calibrated, low-fidelity vortex lattice models to estimate the aerodynamic coefficients [3, 4]. The calibration step is necessary because vortex lattice predictions degrade in quality for cases with large angles of attack or large control surface deflections, which are required for S&C analyses. In an ideal setting, the calibration data are derived from wind tunnel or flight testing. If experimental data are unavailable, high-fidelity computational fluid dynamics (CFD) models may also be employed, although the large number of aerodynamic evaluations required makes it computationally prohibitive to use CFD models to cover the full S&C design space, and CFD models may themselves not be reliable enough for calibration, such as at high angles of attack.

One way to address these challenges is via multifidelity methods that seek to fuse individual models of various fidelity into a single representation of a given quantity of interest [5, 6]. Hierarchical multifidelity methodologies assume that each model in a given set falls somewhere on a spectrum from low to high fidelity, and that there exists a high-fidelity model that represents a “truth” model. Such methods include trust region model management in design optimization [7–9]. Many hierarchical methods use discrepancy functions to correct low-fidelity models with sparse high-fidelity data [10–13]. This approach has been used in the literature in the design of a high-speed civil transport [14], design of a supersonic jet [15, 16], wing design [10], and flight maneuver simulations [17]. Another hierarchical multifidelity methodology is co-kriging [18], where data from two or more models are combined to train a single Gaussian process surrogate model. Co-kriging also allows for the use of gradients as a secondary source of information; examples of its use in the aircraft simulation and design literature include the design of a supersonic jet [19] and for combining computational and experimental data [20].

In this paper, we use a non-hierarchical multifidelity approach; that is, an approach that represents the fidelity of a model as a function of where that model is evaluated in the domain [21–23]. This allows the ordering of a set of models by fidelity to change throughout the domain and does not assume a “truth” model. It also allows for incorporation of information sources other than computational models (e.g., experimental data) and for quantification of uncertainty in the fused multifidelity estimates. Our approach uses the notion of fidelity function as proposed in [22] to quantify our confidence in a particular information source. The main contribution of this paper is to develop the end-to-end methodology that translates these fidelity functions to practical use in the multidisciplinary design setting. We achieve this by proposing a methodology that combines the fidelity functions with other sources of uncertainties, uses surrogates to achieve uncertainty propagation through a coupled multifidelity analysis, and quantifies uncertainty on design quantities of interest. A second contribution of this paper is to illustrate concretely how a multifidelity formulation benefits multidisciplinary design through explicit representation of uncertainty. This illustration is achieved via a challenging problem that goes beyond the academic examples found in much of the existing literature. While specific conclusions can be drawn only about the selected aircraft example, the results point to generalizable conclusions that are relevant to other multidisciplinary design problems.

Section II of this paper describes the multifidelity methodology, which uses Gaussian process models together with a quantification of model fidelity that informs the multifidelity model fusion. Section III presents the example of BWB S&C analysis; it describes the disciplinary models used to estimate center of gravity limits and the quantification of their uncertainties. The problem formulation includes multiple information sources for estimating the aircraft’s aerodynamic coefficients. Section IV presents the results of applying the multifidelity modeling and uncertainty quantification to estimate probability density functions of the performance metrics of interest, namely the fore and aft center of gravity limits and the center of gravity travel range. Finally, Section V concludes the paper.

II. Modeling for Analysis Under Uncertainty

As discussed in the introduction, the main contribution of this paper is an end-to-end methodology that enables multifidelity analysis and uncertainty quantification for a coupled multidisciplinary problem, tackling the challenges of high computational cost and disparate data sources that provide information unevenly over the design space. The methodology weaves together a number of existing elements from the literature, which are described in this section. Section II.A presents an overview of Gaussian process regression, which is used to build surrogate models of the analysis disciplines and provides a platform for synthesizing estimates from multiple information sources. Section II.B presents the model for representing and combining uncertainties, and Section II.C presents the method for computing fused

multifidelity estimates. Section II.D details how the elements come together to create the overall proposed methodology.

A. Gaussian process regression

Gaussian processes have gained prominence in the surrogate modeling and machine learning communities due to their ability to model complex, multidimensional surfaces while simultaneously providing an explicit measure of confidence in their predictive outputs [24, 25]. We use a standard Gaussian process modeling approach to create surrogates for each disciplinary model. We summarize the key elements of the approach here in order to set notation.

Given an input space $\mathcal{D} \subseteq \mathbb{R}^d$ and an input vector $\mathbf{x} \in \mathcal{D}$, we wish to create a surrogate model of the output function $f(\mathbf{x}) : \mathcal{D} \rightarrow \mathbb{R}$. In our setting, the function f represents a scalar quantity of interest that relates to design performance metrics and constraints. We treat each such quantity of interest separately.

A Gaussian process is a function

$$g(\mathbf{x}) \sim \mathcal{GP}(m(\mathbf{x}), k(\mathbf{x}, \mathbf{x})) \quad (1)$$

with mean function $m(\mathbf{x})$ and covariance function $k(\mathbf{x}, \mathbf{x}')$. The mean function describes the trends in the output space while the covariance function encodes the relationship between two points, \mathbf{x} and \mathbf{x}' , in the input space \mathcal{D} .

The posterior prediction of the Gaussian process can be explicitly derived. Let X denote a matrix of N training points,

$$X = \begin{bmatrix} | & | & \cdots & | \\ \mathbf{x}_1 & \mathbf{x}_2 & \cdots & \mathbf{x}_N \\ | & | & & | \end{bmatrix}, \quad (2)$$

where each $\mathbf{x}_j \in \mathcal{D}$ is a training point in the design space. Let $\mathbf{f} = [f_1, f_2, \dots, f_N]^T$ be the column vector containing the corresponding values of the quantity of interest computed by the function being approximated (that is, $f_j = f(\mathbf{x}_j)$, the quantity of interest evaluated at the design point \mathbf{x}_j). The Gaussian process prediction at a test point $\mathbf{x}^* \in \mathcal{D}$ is given by

$$\mu_{GP}(\mathbf{x}^*) = m(\mathbf{x}^*) + k(\mathbf{x}^*, X)k(X, X)^{-1}\mathbf{f} \quad (3)$$

$$\sigma_{GP}(\mathbf{x}^*) = k(\mathbf{x}^*, \mathbf{x}^*) - k(\mathbf{x}^*, X)k(X, X)^{-1}k(X, \mathbf{x}^*), \quad (4)$$

where $\mu_{GP}(\mathbf{x})$ is the posterior mean and $\sigma_{GP}(\mathbf{x})$ is the posterior standard deviation. In (3) and (4), $k(X, X)$ indicates the $N \times N$ covariance matrix whose ij th entry is given by $k(x_i, x_j)$.

The models developed in this paper use a zero prior for the mean, $m(\mathbf{x}) = 0$, and the square exponential with automatic relevance determination for the covariance function:

$$k(\mathbf{x}, \mathbf{x}') = \sigma^2 \exp\left(-\sum_{k=1}^d \frac{\|x_k - x'_k\|_2^2}{2\ell_k^2}\right), \quad (5)$$

where x_k denotes the k th entry of the design vector \mathbf{x} . Maximum likelihood regression is used to compute the values of the hyperparameters σ and ℓ_1, \dots, ℓ_d .

B. Modeling multiple information sources

For a given quantity of interest f we consider n information sources available to inform its prediction. For each information source, we construct a Gaussian process model as described in Section II.A using training data generated from that information source (e.g., simulation data or experimental data). The Gaussian process model for information source i has mean $\mu_{GP,i}(\mathbf{x})$ (Eq. 3) and variance $\sigma_{GP,i}^2(\mathbf{x})$ (Eq. 4). This variance is a quantification of the uncertainty arising from the surrogate modeling process—it reflects uncertainty in the Gaussian process model prediction away from a training point.

To characterize the uncertainty due to the underlying information sources themselves, we draw on the definition of a fidelity function, introduced in [22]. For each information source $i = 1, \dots, n$, define the fidelity function $\sigma_{f,i}(\mathbf{x})$. This fidelity function quantifies our confidence in the underlying information source data, using a standard deviation of the predictions from the true value of $f(\mathbf{x})$. Note that the probability density function from which $\sigma_{f,i}(\mathbf{x})$ is computed is usually unknown and in practice is either assumed or inferred from expert opinion. The variance $\sigma_{f,i}^2(\mathbf{x})$ is a quantification of the uncertainty associated with the fidelity of information source i .

Our approach combines these two estimates of uncertainty, $\sigma_{\text{GP},i}$ and $\sigma_{t,i}$, to form our overall surrogate for information source i , which we denote \tilde{f}_i . The surrogate $\tilde{f}_i(\mathbf{x})$ has mean $\mu_{\text{GP},i}(\mathbf{x})$ and total variance

$$\sigma_{t,i}^2(\mathbf{x}) = \sigma_{\text{GP},i}^2(\mathbf{x}) + \sigma_{f,i}^2(\mathbf{x}), \quad (6)$$

which is computed by summing the Gaussian process and fidelity variances. Note that the Gaussian process standard deviation, $\sigma_{\text{GP},i}$, is zero at the training points since the training data are treated as exact observations of the information source. However, the total variance of $\tilde{f}_i(\mathbf{x})$ cannot be lower than the fidelity variance. If the surrogate is perfectly trained, i.e., the Gaussian process standard deviation is zero, the total standard deviation will be equal to the fidelity standard deviation. This prevents a surrogate from being treated as too reliable simply because it is better trained. Likewise, including the Gaussian process standard deviation in the total standard deviation prevents badly trained surrogates, or estimates at points far outside of the training set, from being treated as too reliable, even if the fidelity variance is small.

C. Multifidelity fused estimates

Our multifidelity estimate for the quantity of interest $f(\mathbf{x})$ incorporates all available information sources while also taking into account the degree of confidence that the designer has in each model. The multifidelity estimate is constructed using a weighted sum of estimates from each information source, where the weighting is inversely proportional to the model variance so that high-confidence models are weighted more heavily. This weighting uses long-established theory on combining probability distributions [26]. The multifidelity mean estimate is given by a variance-weighted sum of the individual mean estimates:

$$\bar{\mu}(\mathbf{x}) = \bar{\sigma}^2(\mathbf{x}) \sum_{i=1}^n \frac{\mu_{\text{GP},i}(\mathbf{x})}{\sigma_{t,i}^2(\mathbf{x})}, \quad (7)$$

where

$$\bar{\sigma}^2(\mathbf{x}) = \left(\sum_{i=1}^n \frac{1}{\sigma_{t,i}^2(\mathbf{x})} \right)^{-1} \quad (8)$$

is the multifidelity estimate of the total variance, computed by taking a weighted sum of the individual, total model variances.

Equations (7) and (8) follow the theory in [26], assuming that each information source is independent. If the dependencies among information sources can be reliably estimated (e.g., through modeling the correlations in their various discrepancies from truth as is done in [27]) then the multifidelity estimates can be modified accordingly, again using the theory in [26].

D. Multifidelity methodology

Figure 2 depicts the overall end-to-end multifidelity methodology proposed in this paper. This methodology combines the elements described above—the notion of non-hierarchical multifidelity formulations to fuse disparate data, the definition of fidelity functions to quantify information source uncertainty, and Gaussian process models to reduce computational cost—and combines them with a coupled multidisciplinary analysis formulation and uncertainty propagation via Monte Carlo sampling.

As the example problem presented in the remainder of the paper demonstrates, the proposed approach addresses many of the challenges discussed in Section I. Yet, the proposed approach has a number of limitations and drawbacks. First, the definition of the fidelity functions may be difficult. Trusted data sources are invaluable in quantifying the fidelity, but ultimately the task must inject expert opinion. On the one hand, this provides a way to bring designer experience to bear in the approach, but on the other hand it introduces subjectivity to the approach. Second, the proposed approach is based on probabilistic representations of uncertainty. This choice was made because it translates into a computationally tractable and relatively simple algorithm, and because the probabilistic representations can be justified based on statistical theory such as the Principle of Maximum Entropy [28] as discussed in more detail in [21]. However, we note that other ways to represent uncertainty, such as possibility theory, Dempster-Shafer evidence theory, imprecise probabilities, and interval analysis [29–32], are preferred among some parts of the community. Third, our approach inherits the computational difficulties associated with Gaussian process regression. In particular, the task of determining the hyperparameters is often numerically ill-conditioned, especially as the dimension of the parameter space increases. This can translate into a lack of robustness of the resulting surrogate model.

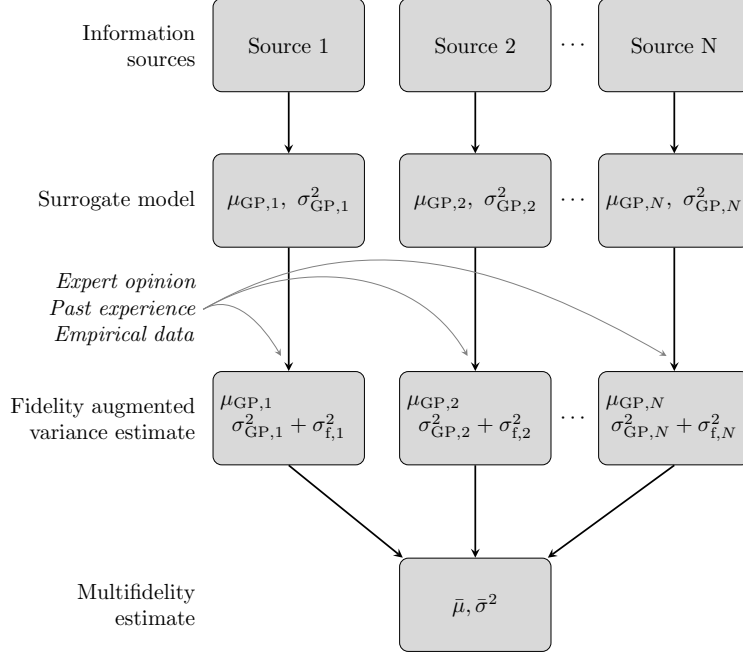


Fig. 2 Our multifidelity methodology combines multiple information sources and augments the variance estimate using expert input and prior knowledge to form the multifidelity estimate.

III. Blended Wing Body Example

Unlike conventional aircraft configurations, the planform of the BWB is driven in large part by the stability and control (S&C) characteristics of the vehicle [2, 33]. The S&C criteria are highly nonlinear due to the three-dimensional nature of the aerodynamic flow and the fact that most of the S&C criteria involve stall conditions. Many aerodynamic analysis methods commonly used for conceptual design are unable to model such flow behaviors, due to their linear formulation or missing physics. This necessitates the use of more expensive high-fidelity analysis to better evaluate S&C constraints of a BWB configuration, yet the computational costs of using only high-fidelity models quickly becomes prohibitive. This section presents an overview of the aerodynamic and S&C models used to analyze an illustrative BWB example configuration.

A. Geometry

The geometry of the BWB is modeled using the Engineering SketchPad (ESP), a parameterized CAD toolkit [34]. The BWB analyzed in this paper is inspired by the ERA-0009H1 planform [35]. The centerbody airfoils are slightly reflexed (inverted NACA 4-series) while the wing airfoils are all symmetric NACA 4-series airfoils. Only the wing and centerbody are modeled, as shown in Figure 3.

The planform, shown in Figure 4, consists of four elements: a centerbody section, a fairing between the centerbody and panel one of the wing, a two-panel wing, and a winglet. Thirteen control surfaces are cut into the centerbody and wing. The inner three are denoted as the inboard (IB) control surfaces while those on the outer wing are the outboard (OB) control surfaces.

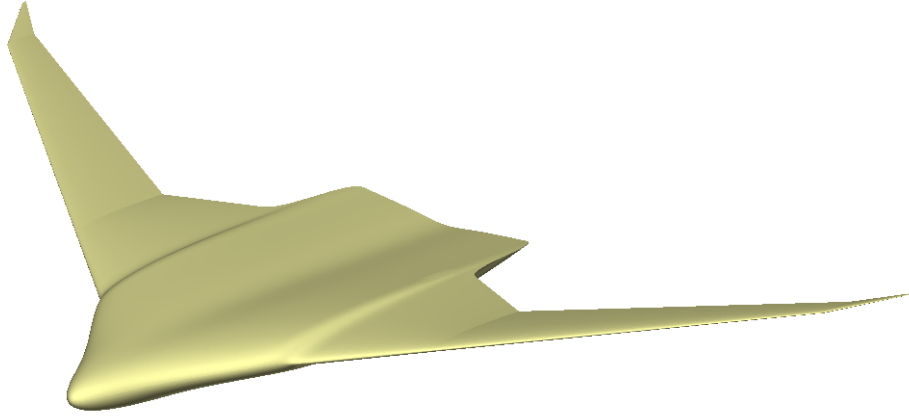


Fig. 3 ESP representation of the BWB geometry used in this work.

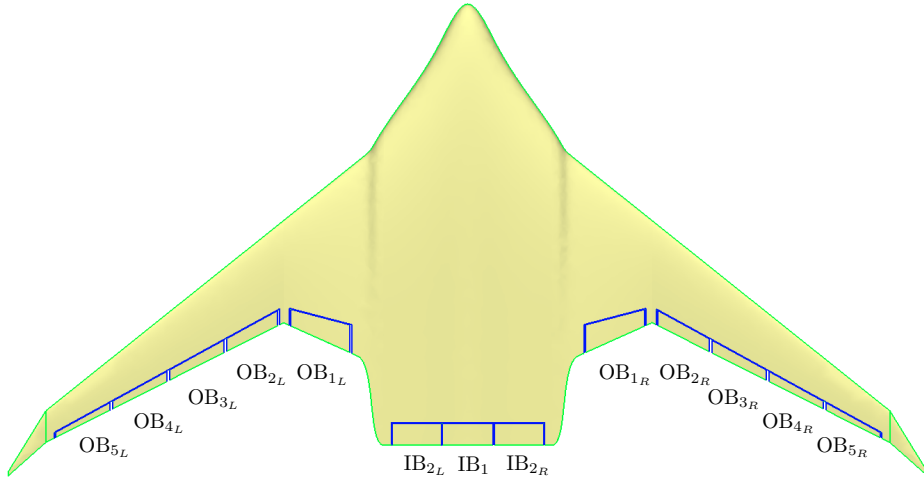


Fig. 4 Top view of the BWB planform with the inboard (IB) and outboard (OB) control surfaces denoted.

B. Aerodynamics

The aerodynamic models compute the lift coefficient, C_L , drag coefficient, C_D , and pitching moment coefficient about the reference point, $C_{m_{ref}}$. The aerodynamic outputs are functions of the Mach number M , the angle of attack α , and the deflections of 7 control surfaces δ_1 (IB₁), δ_2 (IB₂), δ_3 (OB₁), δ_4 (OB₂), δ_5 (OB₃), δ_6 (OB₄), and δ_7 (OB₅). Together these inputs make up the vector \mathbf{x}_{aero} :

$$\mathbf{x}_{aero} = \left[M \quad \alpha \quad \delta_1 \quad \delta_2 \quad \delta_3 \quad \delta_4 \quad \delta_5 \quad \delta_6 \quad \delta_7 \right]^T \quad (9)$$

Since only the longitudinal S&C characteristics are analyzed in this work, the left and right control surfaces are combined. Thus, a deflection of δ_1 is equivalent to deflecting both OB_{1L} and OB_{1R} in Figure 4. After this simplification, the analysis has $n_\delta = 7$ control surfaces.

Four aerodynamic information sources are used to analyze the BWB: a vortex lattice model, a CFD implementation of the Euler equations, a CFD implementation of the RANS equations, and a notional database of wind tunnel data. No truth model is available for the aerodynamic quantities as estimated by each information source; therefore, each quantity from each model is assigned a fidelity function. As described in Section II.B, these fidelity functions quantify expert opinion about the predictive capability of the information sources with respect to the BWB configuration being analyzed.

Vortex Lattice Aerodynamic Model

The vortex lattice code used for the present work is Athena Vortex Lattice (AVL)*. The AVL representation of the BWB and an example solution are shown in Figure 5. A constant viscous drag of 85 counts is added across all points to align the AVL prediction of the drag with that of the RANS prediction at 4 degrees angle of attack at Mach 0.2. The

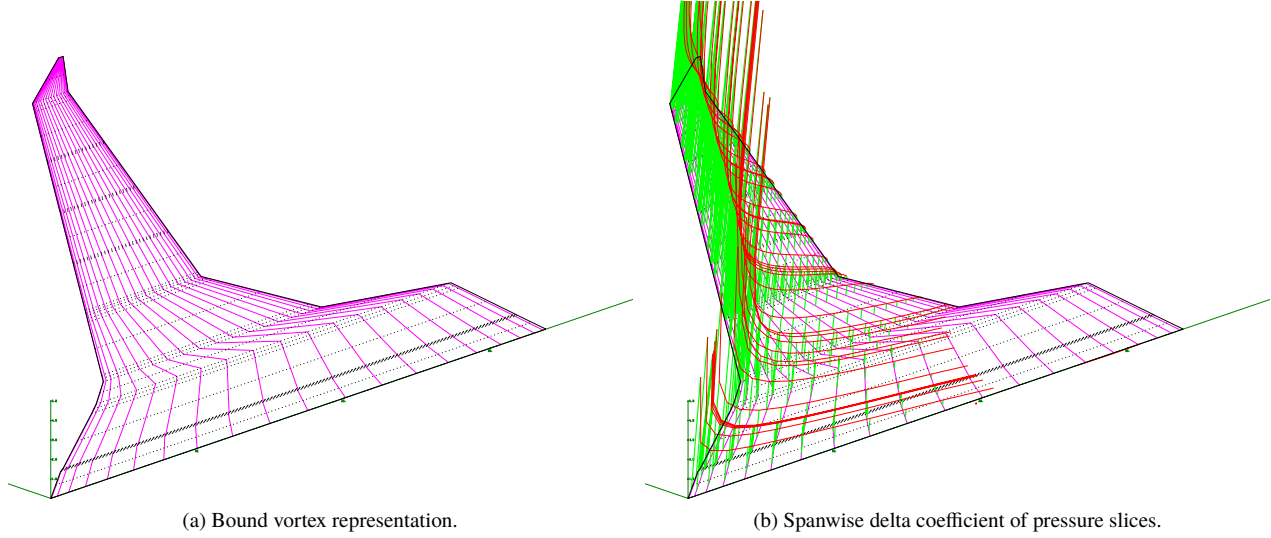


Fig. 5 AVL half planform and solution.

AVL fidelity functions are defined for the AVL estimates of C_L , C_D and $C_{m_{ref}}$. The fidelity standard deviations are chosen to have linear growth proportional to the value of the quantities of interest, representing a decrease in confidence in AVL estimates with increasing angle of attack:

$$3\sigma_{f,C_L}^{AVL}(\mathbf{x}_{aero}) = 0.1|C_L| + 0.1 \quad (10)$$

$$3\sigma_{f,C_D}^{AVL}(\mathbf{x}_{aero}) = 0.8C_D \quad (11)$$

$$3\sigma_{f,C_{m_{ref}}}^{AVL}(\mathbf{x}_{aero}) = 0.1|C_{m_{ref}}| + 0.1 \quad (12)$$

Note that these fidelity functions are constructed for the purpose of the present example, based on expert opinion and other available estimates of the aerodynamic coefficients. These fidelity functions should be considered illustrative; other choices are possible.

Euler Aerodynamic Model

The Euler solver used in this work is the SU2 CFD code [36]. The mesh generation uses ESP for the surface and AFLR3 for the volume meshes[†]. Figure 6 shows an example pressure coefficient solution for a Mach number of 0.2 and an angle of attack of 5 degrees. To account for viscous effects, a constant drag offset of 40 counts is applied. This value was chosen to bring the Euler prediction of the C_D up to the RANS prediction at a Mach number of 0.2 at 4 degrees angle of attack.

Like the AVL fidelity functions, the Euler fidelity functions are chosen to have linear growth proportional to the value of the quantities of interest, again representing increasing uncertainty with increasing angle of attack:

$$3\sigma_{f,C_L}^{Euler}(\mathbf{x}_{aero}) = 0.07|C_L| + 0.07 \quad (13)$$

$$3\sigma_{f,C_D}^{Euler}(\mathbf{x}_{aero}) = 0.5C_D \quad (14)$$

$$3\sigma_{f,C_{m_{ref}}}^{Euler}(\mathbf{x}_{aero}) = 0.07|C_{m_{ref}}| + 0.07 \quad (15)$$

* AVL v3.36 <http://web.mit.edu/drela/Public/web/avl/>

[†] <http://www.simcenter.msstate.edu/software/downloads/doc/aflr3/index.html>

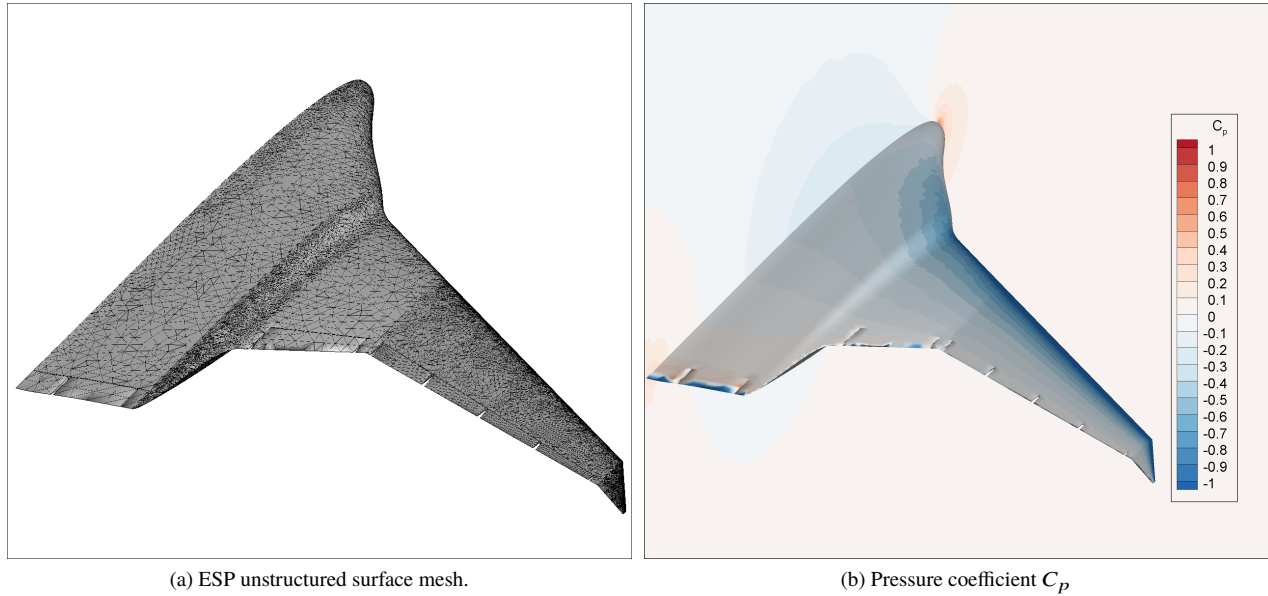


Fig. 6 Euler mesh and solution for Mach 0.2, 5 degrees angle of attack.

RANS Aerodynamic Model

The RANS solver used in this work is the SU2 CFD code [36]. The mesh generation again uses ESP for the surface and AFLR3 for the volume meshes[‡]. We used a Reynolds number of 85 million and the Negative Spalart-Allmaras turbulence model. Figure 7 shows an example pressure coefficient solution for a Mach number of 0.2 and an angle of attack of 4 degrees.

The fidelity functions are again chosen such that the fidelity is linearly proportional to the value of the quantities of interest:

$$3\sigma_{f,C_L}^{\text{RANS}}(\mathbf{x}_{aero}) = 0.05|C_L| + 0.05 \tag{16}$$

$$3\sigma_{f,C_D}^{\text{RANS}}(\mathbf{x}_{aero}) = 0.1C_D \tag{17}$$

$$3\sigma_{f,C_{m_{ref}}}^{\text{RANS}}(\mathbf{x}_{aero}) = 0.05|C_{m_{ref}}| + 0.05 \tag{18}$$

[‡]<http://www.simcenter.msstate.edu/software/downloads/doc/aflr3/index.html>

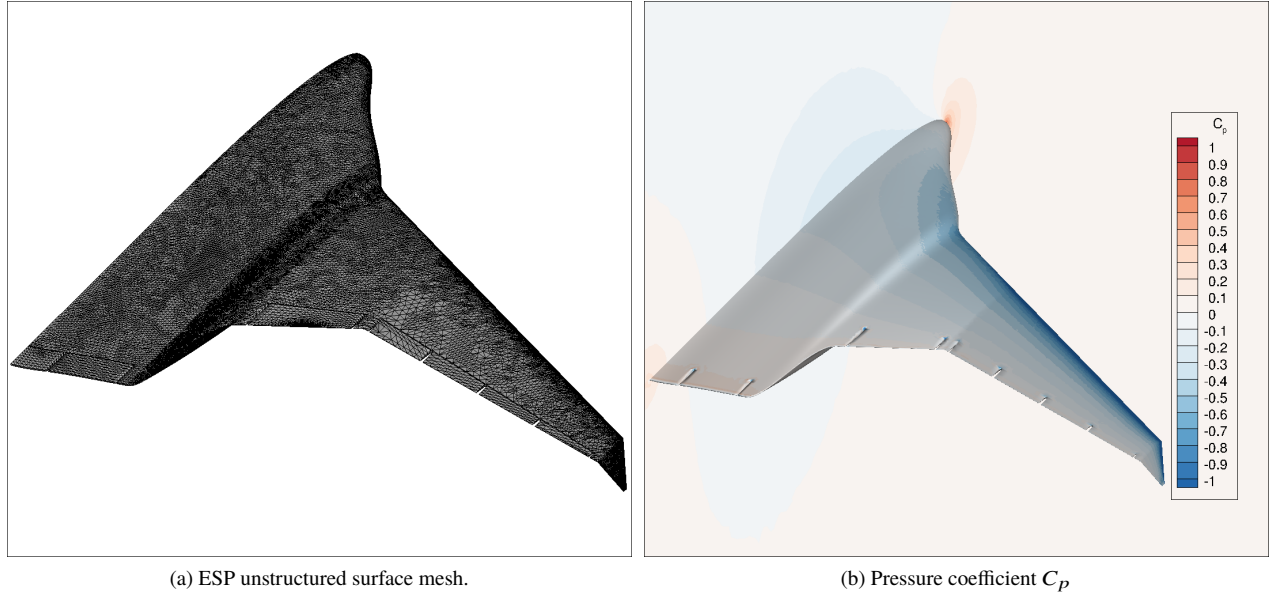


Fig. 7 RANS mesh and solution for Mach 0.2, 5 degrees angle of attack.

Notional Wind Tunnel Aerodynamic Data

The fourth source of aerodynamic information available for the S&C analysis is a wind tunnel database. Here we use notional but representative wind tunnel data, constructed to represent design points that might reasonably be available from a wind tunnel test campaign. The wind tunnel fidelity functions are chosen to be constant for all points in the aerodynamic design space, representing a constant level of confidence in the (notional) data:

$$3\sigma_{f,C_L}^{WT}(\mathbf{x}_{aero}) = 0.01 \quad (19)$$

$$3\sigma_{f,C_D}^{WT}(\mathbf{x}_{aero}) = 5 \times 10^{-4} \quad (20)$$

$$3\sigma_{f,C_{m_{ref}}}^{WT}(\mathbf{x}_{aero}) = 0.01 \quad (21)$$

In this case, the fidelity functions can be thought of as quantifying experimental noise and error.

Aerodynamic Force Calculation

The aerodynamic coefficients are computed in the stability reference frame. The side force, yawing moment, and rolling moment are ignored since the considered S&C cases involve only longitudinal motion. The forces and moments are converted into the body frame (as shown in Figure 8) using the following equations:

$$F_{X_{aero}} = (C_L \sin \alpha - C_D \cos \alpha) S_{ref} \bar{q} \quad (22)$$

$$F_{Z_{aero}} = -(C_L \cos \alpha + C_D \sin \alpha) S_{ref} \bar{q} \quad (23)$$

$$C_{m_{CG}} = C_{m_{ref}} + \frac{F_{Z_{aero}}(x_{CG} - x_{ref}) - F_{X_{aero}}(z_{CG} - z_{ref})}{S_{ref} c_{ref} \bar{q}} \quad (24)$$

$$M_{Y_{aero}} = C_{m_{CG}} S_{ref} c_{ref} \bar{q} \quad (25)$$

Here S_{ref} is the planform area, c_{ref} is the mean aerodynamic chord, \bar{q} is the dynamic pressure, and $(x, y, z)_{ref}$ is the location at which the pitching moment $C_{m_{ref}}$ was computed by the aerodynamic code. The forces in the body frame due to the aerodynamics are denoted by $F_{X_{aero}}$ and $F_{Z_{aero}}$ in the x and z directions, respectively. To compute the pitching moment, the moment coefficient about the reference point, $C_{m_{ref}}$, is transferred to the center of gravity $(x, y, z)_{CG}$. Note that both locations are computed in the body frame. The resulting pitching moment coefficient about the center of gravity is denoted by $C_{m_{CG}}$. This coefficient is then used to compute the moment about the center of gravity due to the aerodynamic forces $M_{Y_{aero}}$.

C. Stability and Control

The goal of the S&C analysis is to compute the flight center of gravity limits and to characterize the controllability of the aircraft. In this work only the longitudinal stability criteria are analyzed. These criteria compute the forward and aft center of gravity limits for the BWB as well as the location of the main landing gear along the longitudinal axis of the vehicle.

We assume that the aircraft is symmetric about the xz plane, quasi-rigid, and fixed mass. Under these assumptions, and only considering accelerations along the pitch axis, the equations of motion in the body axes simplify to the following, as derived in Ref. [37]:

$$m(\dot{U} + g \sin \theta) = F_{X_{aero}} + F_{X_{thrust}} + F_{X_{gear}} \quad (26)$$

$$m(\dot{W} - g \cos \theta) = F_{Z_{aero}} + F_{Z_{thrust}} + F_{Z_{gear}} \quad (27)$$

$$\dot{Q}I_{yy} = M_{Y_{aero}} + M_{Y_{thrust}} + M_{Y_{gear}} \quad (28)$$

Here m denotes the mass of the vehicle, \dot{U} is the acceleration along the x_{body} axis, \dot{W} is the acceleration along the z_{body} axis, g is the acceleration due to gravity, θ is the angle between the ground and the chord line, \dot{Q} is the rotational acceleration about the y axis, and I_{yy} is the moment of inertia about the y axis. The aerodynamic forces and moments, $F_{X_{aero}}$, $F_{Z_{aero}}$, and $M_{Y_{aero}}$ are computed using Equations (22), (23), and (25). The landing gear forces and pitching moment are given by $F_{X_{gear}}$, $F_{Z_{gear}}$, and $M_{Y_{gear}}$. When the aircraft is in the air the gear forces and moment are set to zero.

For the ground-based criteria a three component landing gear configuration is used: a nose gear and two main gear. A diagram of the axis systems is shown in Figure 8.

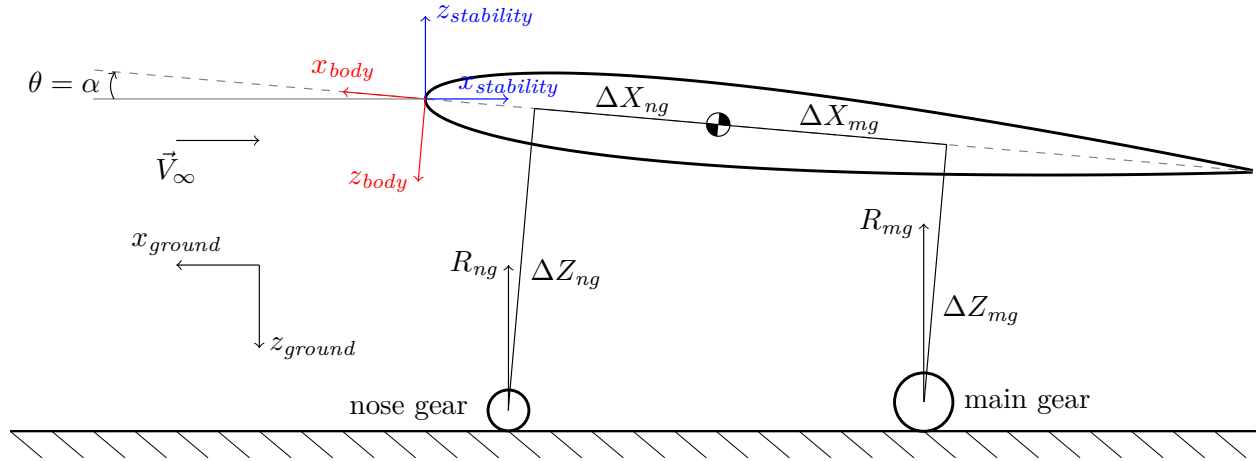


Fig. 8 Axis systems for the BWB S&C analysis on the ground along with the gear reaction forces R_{mg} and R_{ng} . Note this figure is not to scale.

The main gear are modeled as symmetric about the xz plane at a distance ΔX_{mg} along x_{body} and ΔZ_{mg} along the z_{body} axis from the center of gravity. Similarly, the nose gear is a distance ΔX_{ng} along the x_{body} axis and ΔZ_{ng} along the z_{body} axis from the center of gravity. Note that the center of gravity is assumed to be between the nose and main gear, and therefore the distances are taken to be the absolute values of the moment arms between the gear and CG location. By considering only longitudinal motion, the equations of motion in the ground axes, $(x, y, z)_{ground}$, simplify to the following, as derived in Ref. [38]:

$$m\dot{U}_{ground} = \sum F_{X_{ground}} - \mu (R_{ng} + R_{mg}) \quad (29)$$

$$m(-\dot{Q}\Delta X_{mg} \cos \theta - g) = \sum F_{Z_{ground}} - (R_{ng} + R_{mg}) \quad (30)$$

$$\dot{Q}I_{yy} = \sum M_Y + R_{ng} (\Delta X_{ng} - \mu \Delta Z_{ng}) - R_{mg} (\Delta X_{mg} + \mu \Delta Z_{mg}) \quad (31)$$

In the above equations, \dot{U}_{ground} is the acceleration along x_{ground} , R_{ng} is the magnitude of the reaction force of the nose gear, R_{mg} is the magnitude of the total reaction force of the main gear, and μ is the rolling friction coefficient. The

summations are taken over the external forces and moments computed in the body axes. For the BWB these these include the aerodynamic forces given in Equations (22), (23), and (25).

The longitudinal S&C criteria originate from the United States Federal Aviation Regulations (FAR) Part 25. There are four criteria, two for the forward center of gravity limit, one for the aft limit, and one to set the main gear location along the longitudinal axis of the vehicle. We now briefly describe each criterion.

Fly-To-Stall

The fly-to-stall criterion requires that the control system be able to achieve stall. It is evaluated by trimming the aircraft at 1.13 and 1.3 times the stall speed and then flying it to stall with the control devices. The objective of the criterion is to find the furthest forward center of gravity limit such that the aircraft can be controlled to stall. The speed that produces the furthest aft limit is used as the critical speed.

Stall Recovery

After the aircraft flies to stall it must be able to recover at a specified rotation rate. The FAR requires “prompt” recovery, which has been interpreted to mean a recovery rotation rate of at least -5 deg/s^2 [39]. The objective of this criterion is to find the furthest aft center of gravity limit where this rotation requirement is met. The criterion is evaluated at both 1.13 and 1.3 times the stall speed, and with no thrust, idle thrust, and full thrust in order to determine which case is the most critical.

Nose-Wheel Steering

The nose-wheel steering criterion sets the longitudinal location of the main gear. Using Ref. [40], the main gear are placed such that at a minimum 6% of the aircraft’s weight is on the nose gear at maximum takeoff weight. For this criterion, the center of gravity is placed at the aft limit as determined by the free flight cases. The computed main gear location is then propagated through the rest of the ground based analyses. This is done to create the widest possible center of gravity travel range.

Nose-Wheel Liftoff

The nose-wheel liftoff criterion specifies the pitch-up rotation rate of the aircraft during takeoff. A minimum rotation rate of 3 deg/s^2 is required when the pitch control surfaces are fully deflected to give an upward rotation[§]. The computed center of gravity is a forward limit and may be further aft than the fly-to-stall limit.

IV. Results

We now demonstrate our multifidelity methodology on the S&C analysis of the BWB presented in Section III. The four aerodynamic models from Section III.B are used to build multifidelity surrogates for each of the aerodynamic coefficients. The uncertainties in the resulting predictions are then propagated through the S&C analysis to determine the impact of imperfect aerodynamic data on the S&C analysis.

A. Aerodynamic Surrogates

Gaussian process surrogates are built for the aerodynamic analysis, one for each quantity of interest as computed by each model. The surrogates take in the vector \mathbf{x}_{aero} (Equation 9) as input and estimate the output quantities C_L (lift coefficient), C_D (drag coefficient), and $C_{m_{ref}}$ (pitching moment coefficient about the reference point). The number and location of the training data are chosen to reflect the computational expense of the aerodynamic model that generated the training data.

AVL

Latin hypercube sampling [41] is used to select 1200 sample points for surrogate training for AVL using the input variable bounds listed in Table 1. The training bounds are chosen to be slightly larger than the expected inputs to the model during the S&C analysis.

[§]<https://web.archive.org/web/20170301222042/http://adg.stanford.edu/aa241/%0AAircraftDesign.html>

Input	Bounds	Units
$Mach$	[0, 0.4]	None
α	[0, 30]	degrees
δ_1	[-45, 45]	degrees
δ_2	[-45, 45]	degrees
δ_3	[-45, 45]	degrees
δ_4	[-45, 45]	degrees
δ_5	[-45, 45]	degrees
δ_6	[-45, 45]	degrees
δ_7	[-45, 45]	degrees

Table 1 Input variable bounds for the AVL aerodynamic surrogates.

Surrogate models of the AVL estimates for the lift, drag, and pitching moment coefficient without control surface deflections are shown in Figure 9. Both the fidelity (σ_f) and Gaussian process (σ_{GP}) standard deviations are shown. The Gaussian process standard deviation confidence interval is tight for all three coefficients due to the large number of training data. The uncertainty along the α domain is dominated by the fidelity standard deviation computed in Equations 10, 11, and 12, respectively. This behavior is expected due to the low-fidelity nature of AVL. Figure 9d visualizes the pitching moment design space by plotting the pitching moment about various center of gravity locations, given as percentages of the mean aerodynamic chord (MAC).

Euler

The Euler training points are chosen to reflect expected control surface deflections, angles of attack, and Mach numbers during the S&C analysis. The BWB is analyzed with the Euler CFD model at $M = 0.2$ and $M = 0.35$ for angles of attack of 0, 5, 7, 9, 10, 11, 12, and 13 degrees. Further, five control surface groups are defined, as listed in Table 2. Each group is deflected at ± 10 , 20, 30, and 40 degrees in addition to the undeflected case.

Group	Surfaces
1	δ_1, δ_2
2	$\delta_1, \delta_2, \delta_3$
3	$\delta_1, \delta_2, \delta_3, \delta_4$
4	$\delta_1, \delta_2, \delta_3, \delta_4, \delta_5$
5	$\delta_1, \delta_2, \delta_3, \delta_4, \delta_5, \delta_6, \delta_7$

Table 2 Control surface groups for Euler training data.

The $M = 0.2$ cases are reused for $M = 0.0$ in the training of the Euler surrogate models, since Mach numbers of less than 0.2 are expected during the S&C analysis and the $M = 0.2$ cases are considered to be incompressible. Of the 656 cases run, 536 converged to a satisfactory density residual value of 10^{-7} . After removal of the non-converged cases and reusing the Mach 0.2 data to represent Mach 0.0, the training set for the Euler surrogates contains 855 points.

The resulting lift, drag, and pitching moment coefficient polars are shown in Figure 10 for a Mach number of 0.2 with no control surface deflections. The total predicted standard deviation is dominated by the fidelity through the middle of the domain, where the Euler data was most heavily concentrated. At the edges of the α domain the Gaussian process standard deviation dominates, as there are few training points in these areas.

RANS Estimates

The RANS model is used to analyze the BWB at $M = 0.2$ for 0, 4, 8, 12, 16, and 20 degrees angle of attack. The control surface groups listed in Table 3 are deflected at ± 40 degrees in addition to the undeflected case. The data are reused for $M = 0.0$ and $M = 0.3$, as all three Mach numbers are considered to be incompressible. This results in a

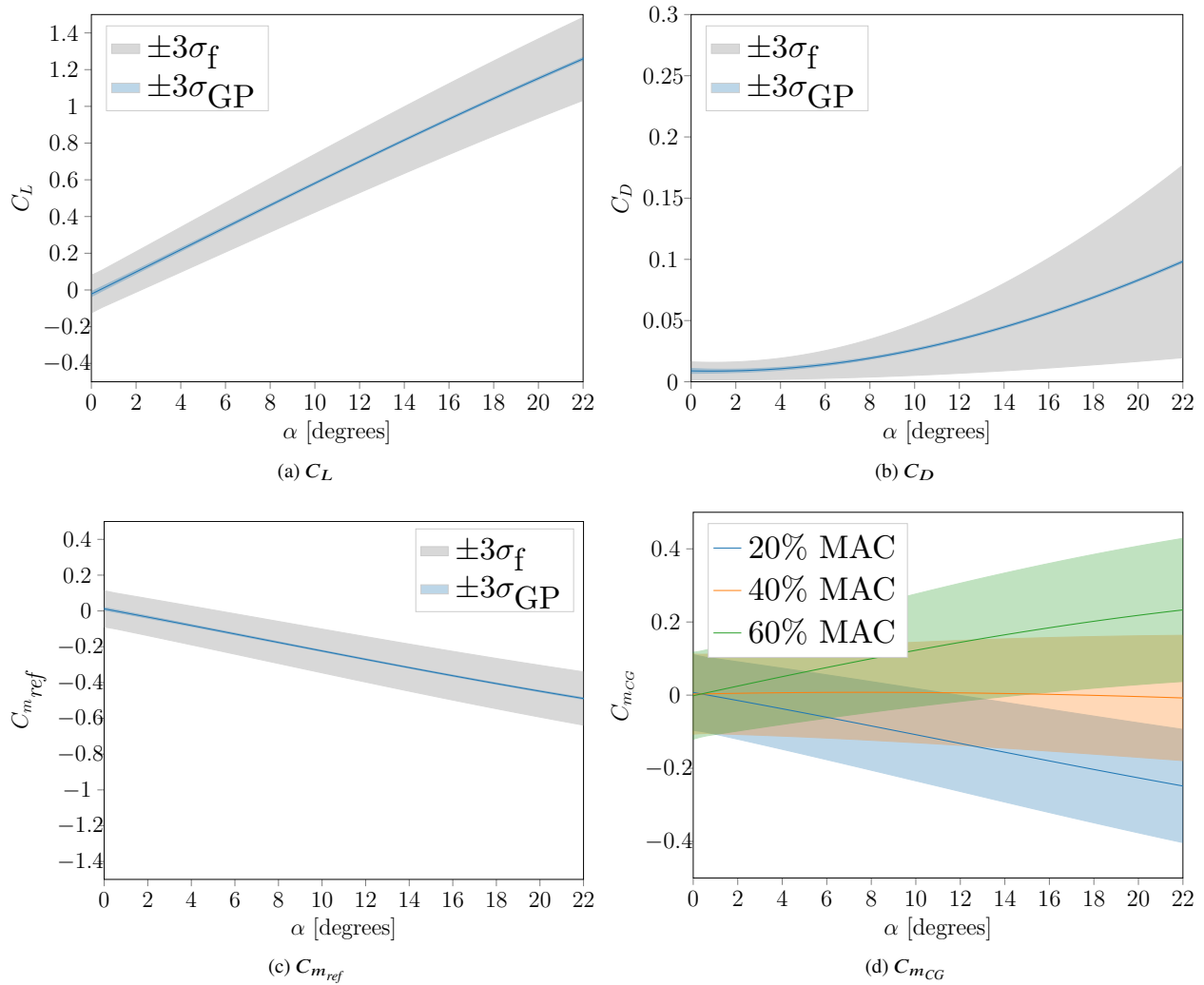


Fig. 9 Surrogate model estimates of the AVL aerodynamic coefficients at Mach 0.20 with $\pm 3\sigma_f$ and $\pm 3\sigma_{GP}$ confidence bounds with no control surface deflections.

training set of 90 points. The fidelity functions given in Equations 16, 17, and 18 model the trust we have in the data at each point.

Group	Surfaces
1	$\delta_1, \delta_2, \delta_3, \delta_4$
2	$\delta_1, \delta_2, \delta_3, \delta_4, \delta_5$

Table 3 RANS control surface groups used to build the surrogate model.

Slices of the lift, drag, and pitching moment coefficients are shown in Figure 11 for a Mach number of 0.2 with no control surfaces deflected. At this slice of the Mach dimension, the Gaussian process standard deviation is the largest contributor to the uncertainty over the majority of the α domain, with dips only at the training points. The C_{mCG} space, however (Figure 11d), has almost constant uncertainty across the α domain.

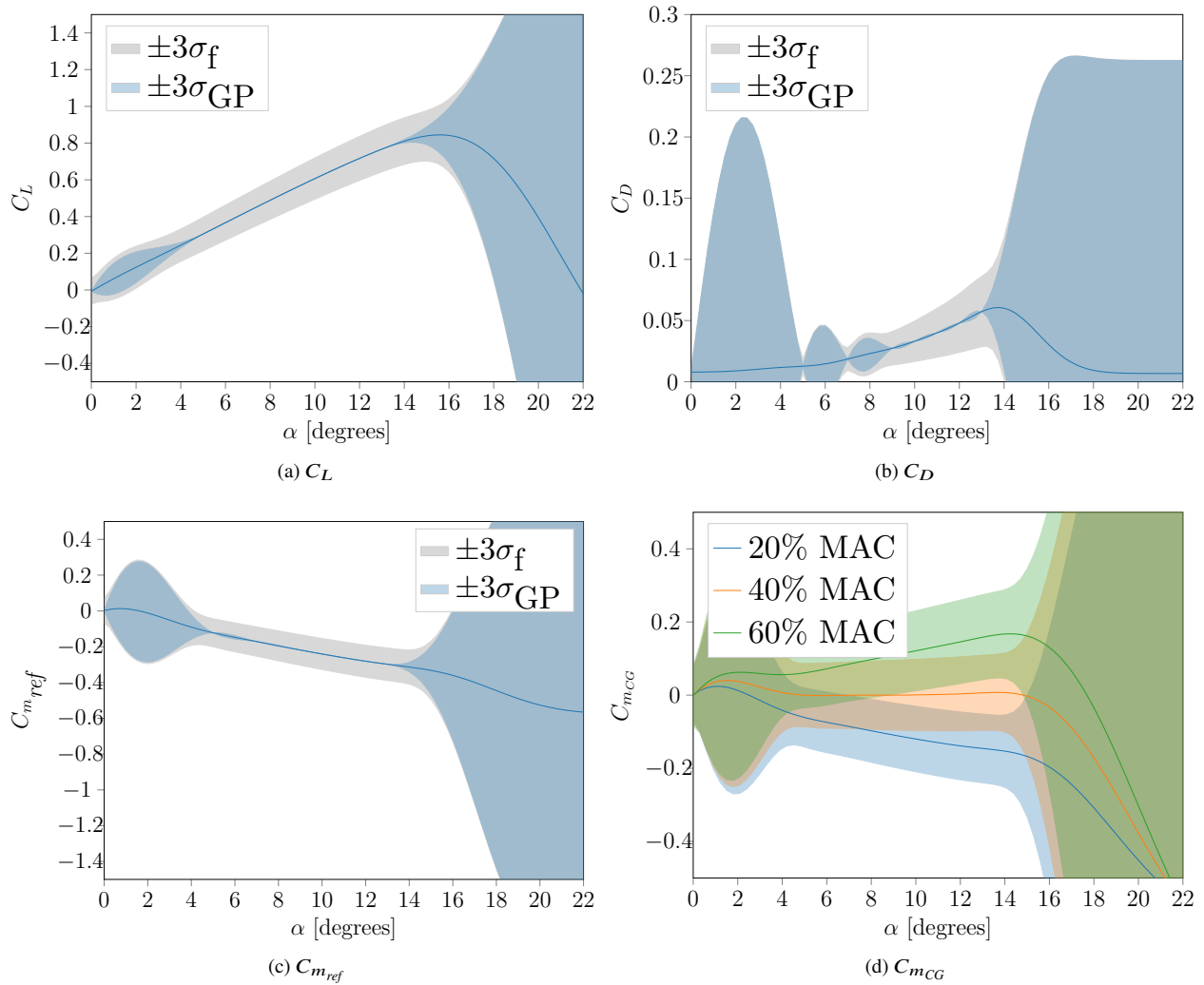


Fig. 10 Surrogate model estimates of the Euler aerodynamic coefficients at Mach 0.20 with $\pm 3\sigma_f$ and $\pm 3\sigma_{GP}$ confidence bounds with no control surface deflections.

Wind Tunnel

The wind tunnel data are constructed to reflect a typical wind tunnel entry. The training data are comprised of notional measurements at Mach 0.0, 0.2, and 0.3 for 0, 12, 16, and 20 degrees angle of attack and three control surface deflections. The control surface groups listed in Table 4 are deflected at 0 and ± 40 degrees. In total, 40 points are in the training set. Noise and error in the wind tunnel measurements are modeled using the fidelity functions given in Equations 19, 20, and 21.

Group	Surfaces
1	$\delta_1, \delta_2, \delta_3, \delta_4$
2	$\delta_1, \delta_2, \delta_3, \delta_4, \delta_5$

Table 4 Notional wind tunnel control surface groups used to build the surrogate model.

Slices of the lift, drag, and pitching moment coefficients are shown in Figure 12 for a Mach number of 0.2 with no control surfaces deflected. At this slice of the Mach dimension, the Gaussian process standard deviation is the largest contributor to the uncertainty over the majority of the α domain—that is, we have high confidence in the data

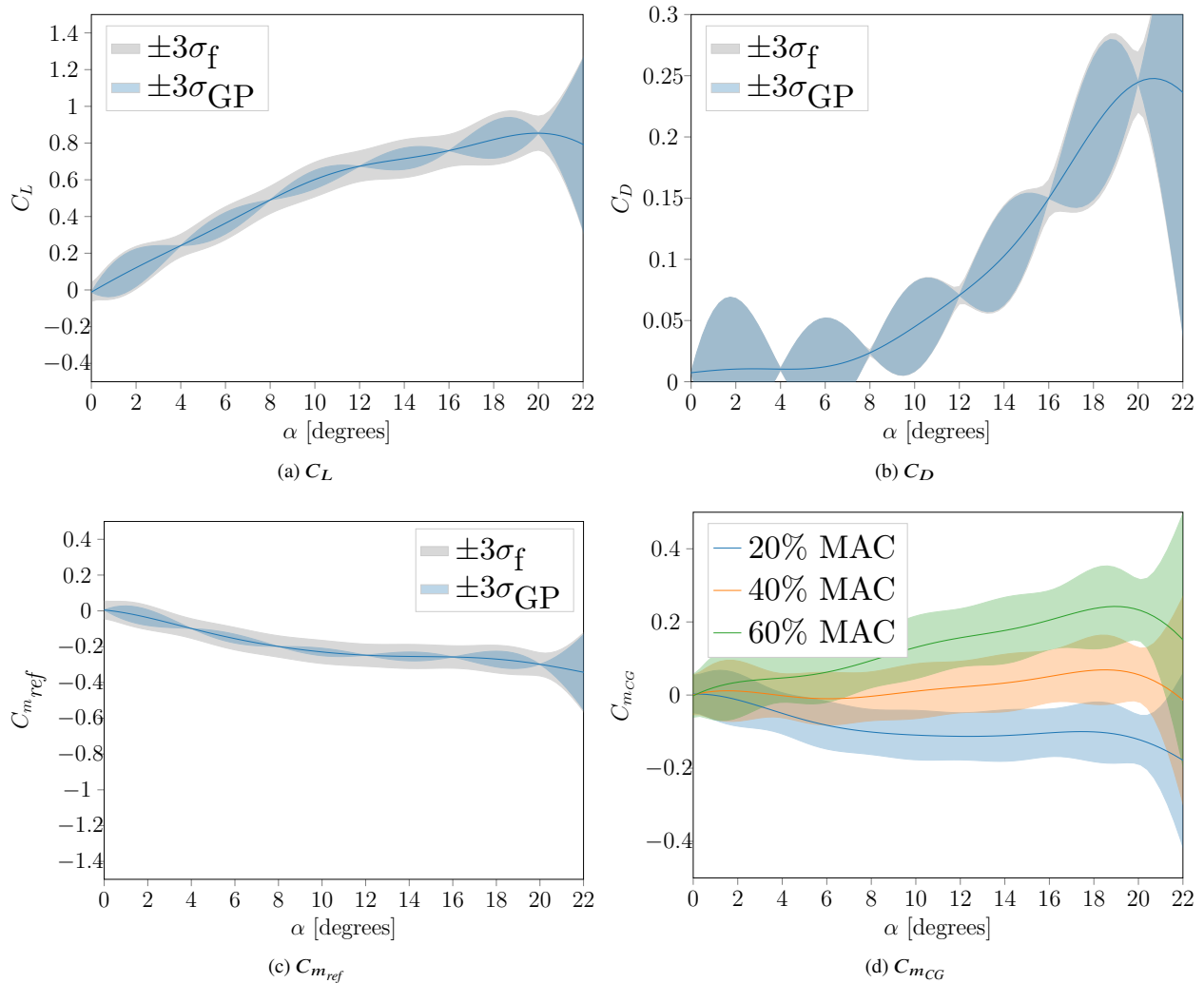


Fig. 11 Surrogate model estimates of the RANS aerodynamic coefficients at Mach 0.20 with no control surface deflections. Confidence bounds of $\pm 3\sigma_f$ and $\pm 3\sigma_{GP}$ are shown.

themselves, but since the data are relatively sparse, points where no training data is present have a large uncertainty. This is especially seen at low values of α .

Multifidelity Aerodynamic Models

Using the methodology developed in Section II, the four aerodynamic models described above are combined into a multifidelity surrogate model for each quantity. To illustrate the methodology, α polars of the lift coefficient C_L as predicted by all four information sources and the multifidelity methodology are shown in Figure 13 at a Mach number of 0.2 and with no control surfaces deflected and in Figure 14 for Mach 0.2 with the four inboard-most control surfaces (δ_1 , δ_2 , δ_3 , and δ_4) deflected downward 20 degrees. At all points along the α axis the multifidelity model reflects the most trusted of the four available aerodynamic information sources. In both cases, the AVL uncertainty is quite large compared to the other available models, so its predictions are weighted lightly in the multifidelity estimate. The wind tunnel model is relied upon in the post-stall region, while the Euler model is relied upon in the upper ranges of the pre-stall α dimension. The RANS model confirms the Euler predictions along the pre-stall portion of the α domain, reducing the total uncertainty in regions where a RANS data point is present. As the wind tunnel model becomes unreliable due to the increasing Gaussian process uncertainty in Figure 14 (i.e., regions where wind tunnel data are unavailable), the RANS model fills the gaps and becomes the primary source.

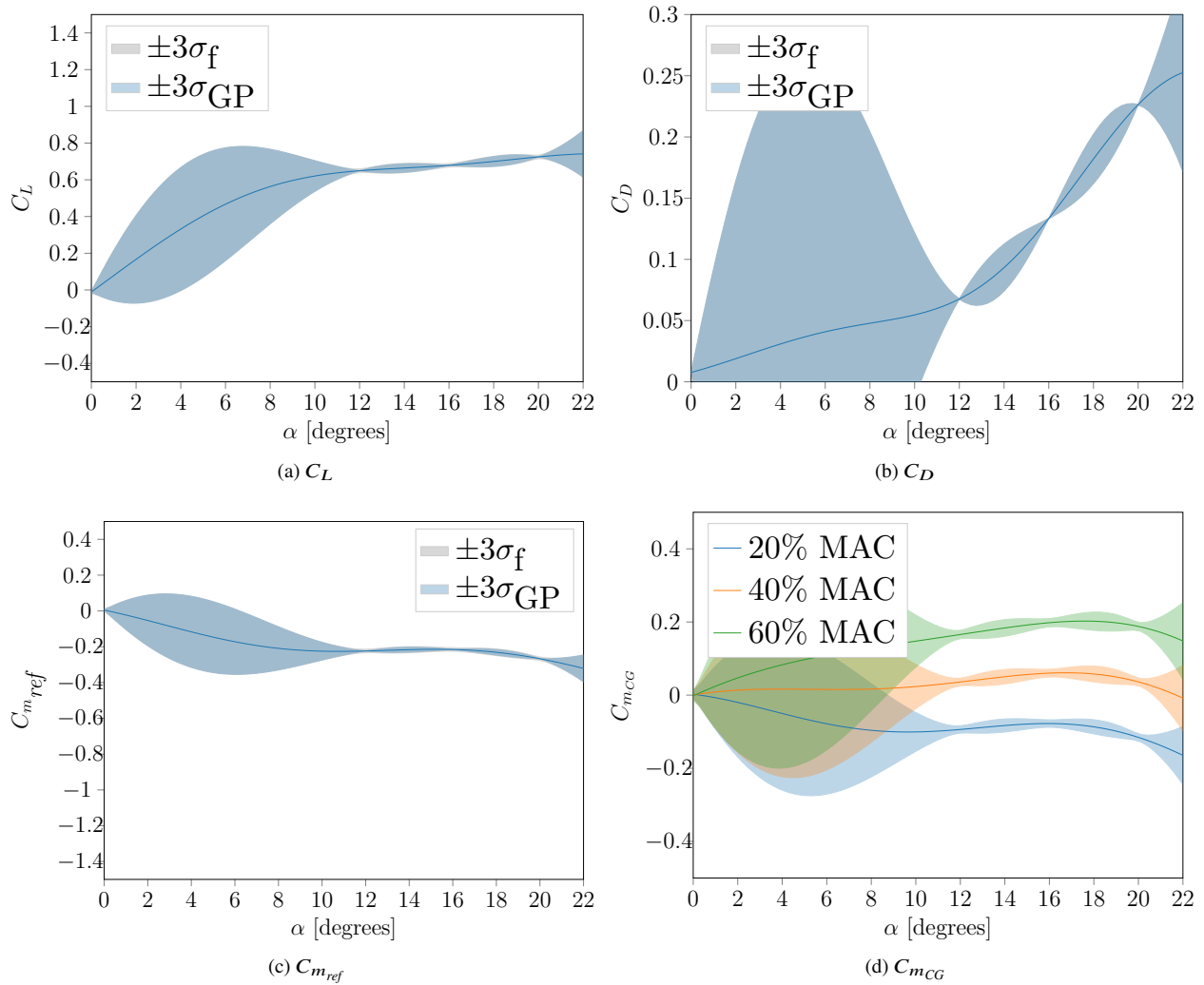


Fig. 12 Surrogate model estimates of the notional wind tunnel aerodynamic coefficients at Mach 0.20 with no control surface deflections. Confidence bounds of $\pm 3\sigma_f$ and $\pm 3\sigma_{GP}$ are shown.

Multifidelity models for all four aerodynamic coefficients are shown in Figure 15 at Mach 0.2 with no control surface deflections and in Figure 16 at Mach 0.2 with the four inboard-most control surfaces deflected downward by 20 degrees. The dips in the standard deviations of the estimates occur in regions where the RANS data are present. In addition, the post-stall curves for both cases closely resemble those of the notional wind tunnel data. This indicates that though the multifidelity surrogate is generating a compromise surface, it naturally reflects the trends of the highest fidelity information source.

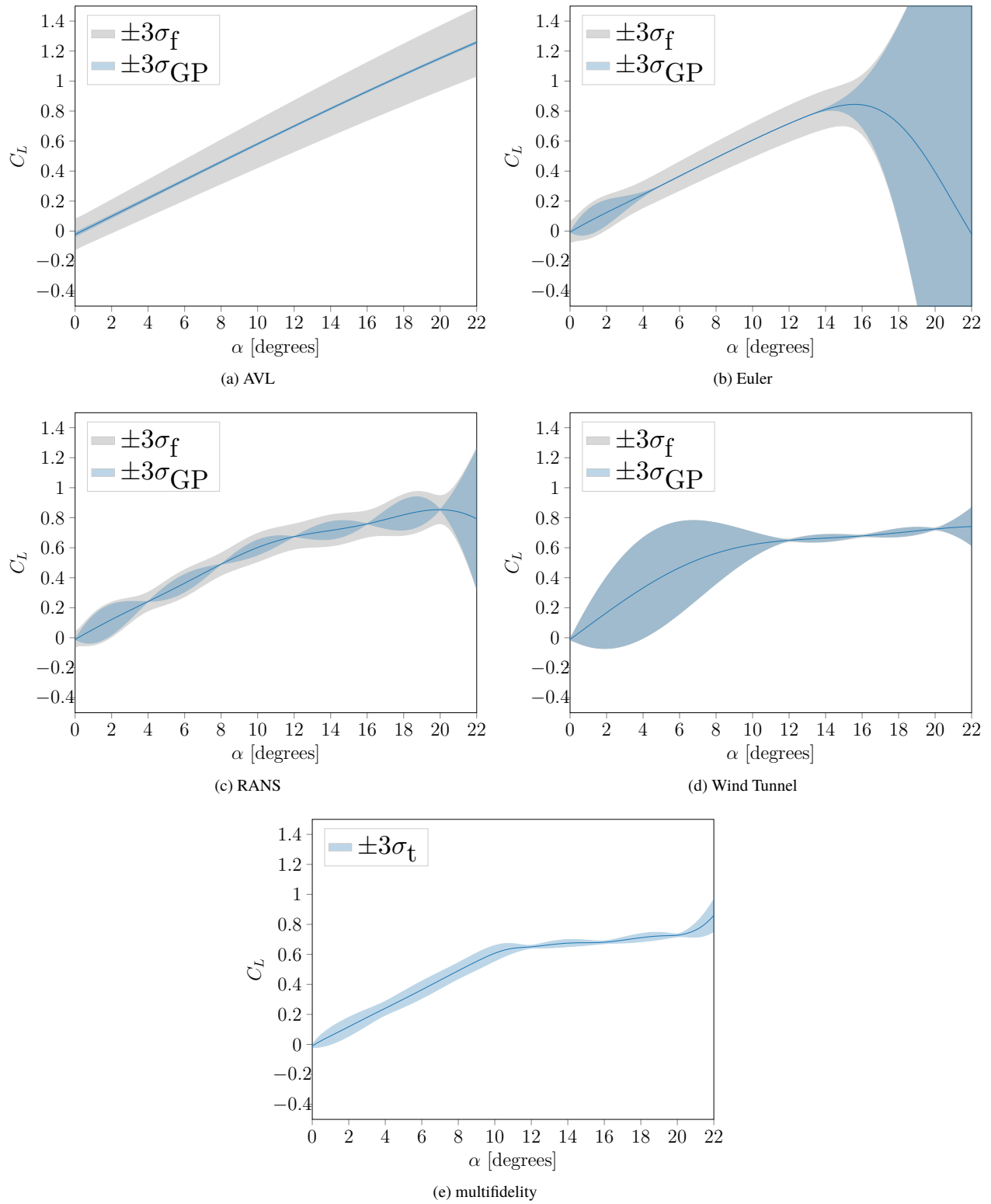


Fig. 13 Formation of the multifidelity C_L estimate by combining AVL, Euler, RANS, and notional wind tunnel data at Mach 0.2 with no control surface deflections.

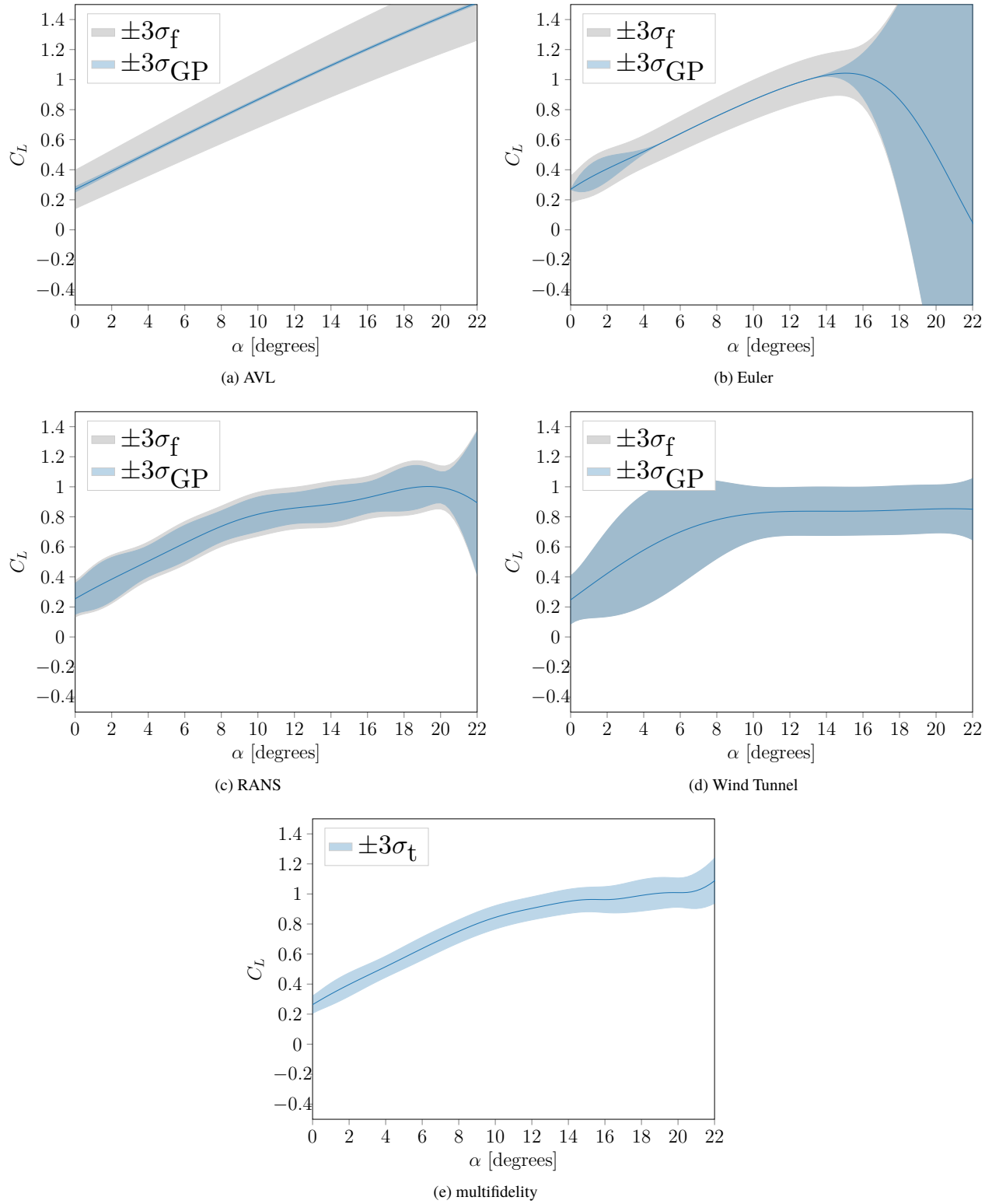


Fig. 14 Formation of the multifidelity C_L estimate by combining AVL, Euler, RANS, and notional wind tunnel data at Mach 0.2 with $\delta_1, \delta_2, \delta_3,$ and δ_4 deflected at 20 degrees.

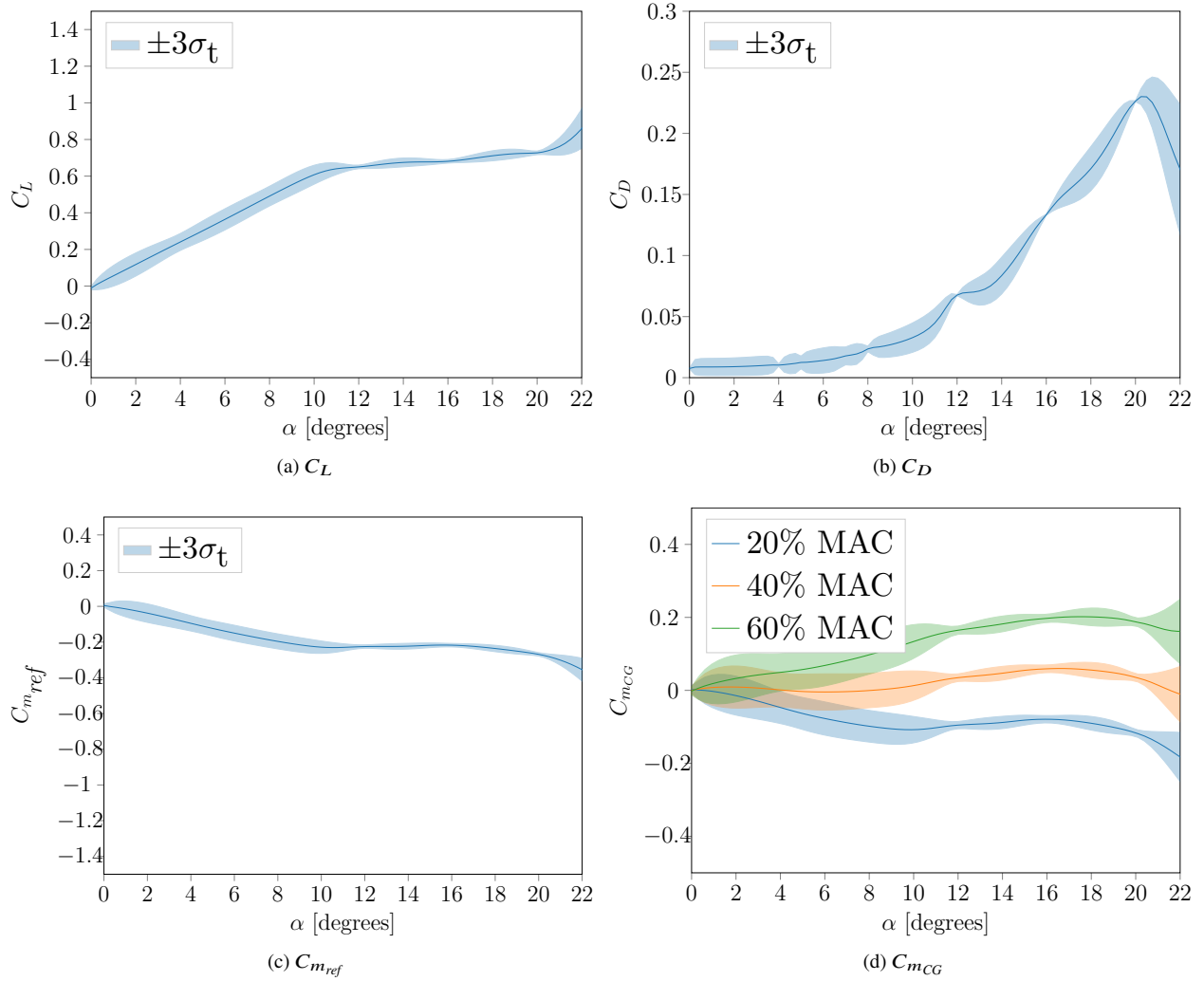


Fig. 15 Multifidelity aerodynamic coefficient estimates at Mach 0.20 with $\pm 3\sigma_f$ and σ_{GP} confidence bounds with no control surface deflections.

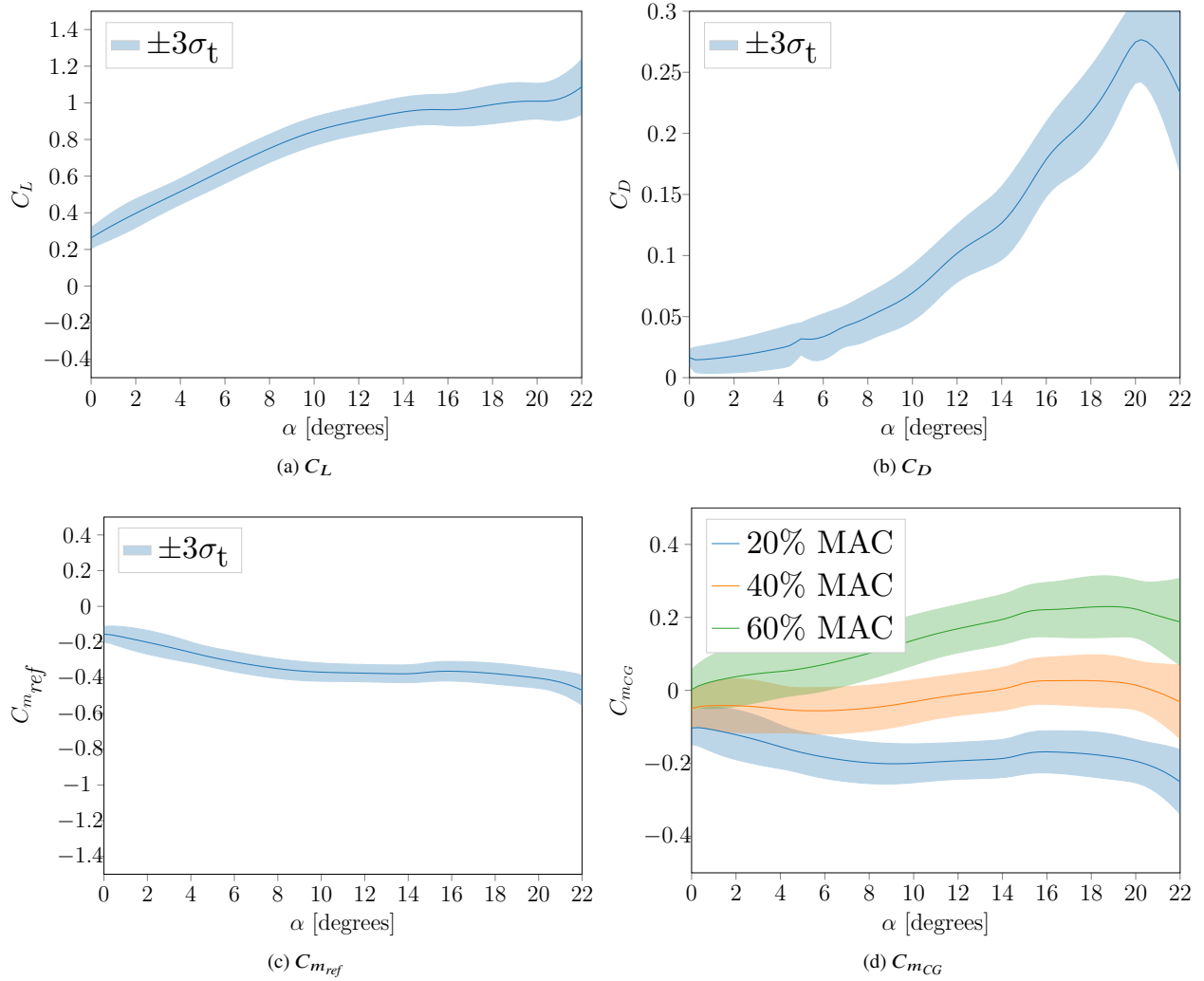


Fig. 16 Multifidelity aerodynamic coefficient estimates at Mach 0.2 with $\delta_1, \delta_2, \delta_3,$ and δ_4 deflected 20 degrees downward.

B. Definition of Uncertain Inputs and Parameters

The goal of the S&C analysis under uncertainty is to determine the impact that the uncertainties in C_L , C_D , and $C_{m_{ref}}$ have on the S&C CG limits. To represent the uncertain aerodynamic data, the S&C analysis under uncertainty is defined by four uncertain inputs: the lift coefficient C_L polar, the drag coefficient C_D polar, the pitching moment coefficient about the aerodynamic reference $C_{m_{ref}}$ polar, and the point at which stall occurs, which is represented by a maximum lift coefficient value $C_{L_{stall}}$. The stall point $C_{L_{stall}}$ is treated as uncertain due to the inability of most computational models, including those used in this study, to accurately predict the point at which the flow separates from the body. Even wind tunnel testing may not accurately capture the stall point, especially if it is preliminary in nature or limited in scope, as is the case in the present work.

The uncertainty in each of these aerodynamic quantities is derived from the models developed in Section III. For a given set of inputs \mathbf{x}_{aero} , each multifidelity Gaussian process surrogate issues a prediction that has a normal distribution, with mean $\bar{\mu}(\mathbf{x})$ (Eq. 7) and standard deviation $\bar{\sigma}(\mathbf{x})$ (Eq. 8). For C_L and $C_{m_{ref}}$, we use these normal distributions directly. For C_D , we modify the distribution to avoid drawing negative drag values (low probability but still possible with the normal distribution). Instead, we use the mean and standard deviation of the drag surrogate to define a triangular distribution with lower bound

$$C_{D,lower} = \max\left(60 \times 10^{-4}, \bar{\mu}_{C_D} - 3\bar{\sigma}_{C_D}\right), \quad (32)$$

upper bound

$$C_{D,upper} = \bar{\mu}_{C_D} + 3\bar{\sigma}_{C_D}, \quad (33)$$

and most probable point $\bar{\mu}_{C_D}$. The stall lift coefficient $C_{L_{stall}}$ is assigned a uniform distribution, with equal probability of taking on any value between 0.6 and 0.7:

$$C_{L_{stall}} \sim U[0.6, 0.7]. \quad (34)$$

For each S&C analysis, we draw one value for $C_{L_{stall}}$, one C_L polar, one C_D polar, and one $C_{m_{ref}}$ polar using these distributions. Noting that the mean and standard deviations vary over the input space \mathbf{x}_{aero} , we draw a consistent polar by sampling the quantile of each distribution. For example, drawing a quantile of 0.5 would define the C_L polar surface following the mean value over the input space, while drawing a quantile of 0.95 would define a C_L polar surface following the mean plus two standard deviation level over the input space, etc. This polar surface is then held constant throughout a single analysis of the four S&C criteria, with a new polar being drawn for each random realization in the Monte Carlo simulation presented in the next subsection.

C. Results

Once the uncertain inputs are defined, an uncertainty propagation study is undertaken to determine the distributions of the S&C quantities of interest. The uncertainty propagation study draws 10,000 independent realizations of the aerodynamic quantities $C_{L_{stall}}$, C_L , C_D and $C_{m_{ref}}$ as described above, and computes the S&C criteria for each realization. The free flight allocation uses surfaces δ_1 , δ_2 , δ_3 , and δ_4 for both trim and control. The takeoff allocation uses δ_1 , δ_2 , δ_3 , δ_4 , and δ_5 for both trim and control. The maximum deflection is chosen to be ± 40 degrees from the undeflected configuration.

To examine the impact of the multifidelity data, the S&C criteria are independently computed using the AVL, Euler, RANS, and wind tunnel derived surrogate models as well as with the multifidelity surrogates. Due to the nonlinear nature of the S&C analysis, some of the cases are not able to find satisfactory locations for the center of gravity to balance the aircraft. In particular, the Fly-to-Stall criterion computed using the Euler derived surrogate models has a 90% failure rate, so 693 samples were collected. Other criteria as computed using the Euler, RANS, and notional wind tunnel derived surrogate models face similar difficulties, with failure rates of about 50%. These high failure rates are due to the nonlinear nature of the S&C criteria as well as the high degree of coupling between the aerodynamic coefficients within the S&C analysis.

Direct comparisons of the means and the ± 2 standard deviations of the S&C criteria as computed using 4000 samples are shown in Figure 17. The multifidelity standard deviations are the smallest of the four aerodynamic models. This is expected as the multifidelity surrogates incorporate all of the available data, thereby lowering the variance of their predictions. Additionally, the multifidelity mean is a combination of the individual fidelity means weighted by their standard deviation, as is expected. The multifidelity mean values are also the smallest of several of the cases, indicating that the reduced variance of the aerodynamic coefficient estimates has led to a reduction in the tails of the S&C criteria distributions.

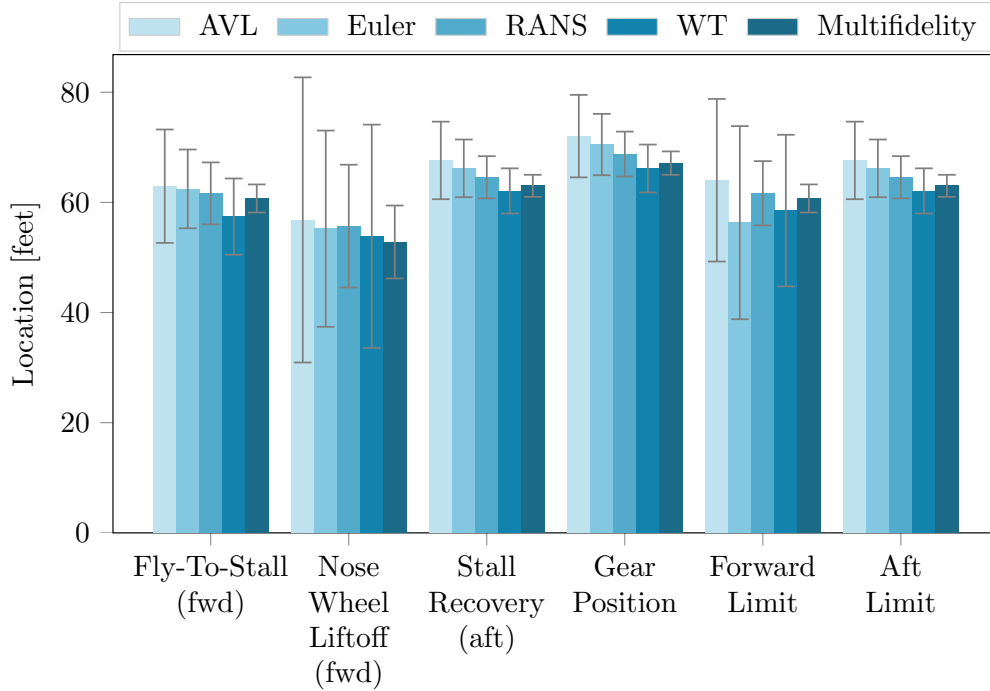


Fig. 17 Comparison of the S&C criteria means with $\pm 2\sigma$ confidence bounds as predicted using each aerodynamic source individually and the multifidelity estimates. All cases are represented using 4000 samples except the Euler Fly-To-Stall case, which uses 693 samples.

To illustrate the difference between the individual and multifidelity models, the samples of each criterion using the lowest-fidelity (AVL) and the multifidelity data are shown in Figures 18 and 19, respectively. Using the AVL derived surrogate models, for all four criteria the range of possible CG and main gear locations is quite large, on the order of at least 25 feet and more than 70 feet for the Nose-Wheel Ltoff criterion. The large uncertainty in the AVL model due to its low-fidelity nature has resulted in high-variance outputs. In contrast, the multifidelity derived CG and main gear locations, in Figure 19, have much smaller ranges, on the order of 20 feet at most.

The forward and aft limit probability density histograms are shown in Figure 20 for both the AVL and multifidelity predictions. Note that the aft limit histograms are the same as the stall recovery histograms in Figures 18b and 19b, since stall recovery is the only aft CG criterion. The forward limit histograms are computed by taking the maximum of the Fly-To-Stall and Nose-Wheel Ltoff CG limit locations for each sample. Note that for both cases, the forward limit histograms are similar to the Fly-To-Stall criterion histograms, indicating that this is the critical criterion for the majority of the samples.

By subtracting the forward limit samples from the aft limit samples, CG travel range histograms can be computed. The CG travel range results are important as they give insight into the overall controllability of the design. A large, positive CG travel range is desirable as it increases the flexibility of the operator in loading the aircraft with fuel and cargo and enlarges the flight maneuver envelopes. On the other hand, a small, or negative, CG travel range indicates that the aircraft will be difficult or impossible to load and control. Therefore, estimating the CG range with confidence is a key indicator for closing the design.

The CG travel range histograms are shown in Figures 20e and 20f. The AVL derived results are concentrated around positive 5 feet but have a long tail out into the negative CG range. In contrast, the multifidelity derived results are tighter, concentrating the majority of the probability mass between 0 and 4 feet of CG range, with a small number of samples having a negative CG range. These results directly show the impact of using multifidelity estimates on the S&C analysis. By incorporating all of the available data, the variance of our estimates of the S&C criteria are reduced, and the probability of the CG range being negative is reduced significantly.

These results also draw attention to the fact that the S&C analysis is only one part of a much larger system. For example, in practice the Nose-Wheel Ltoff criteria can be made less critical (to a point) by allowing the aircraft to

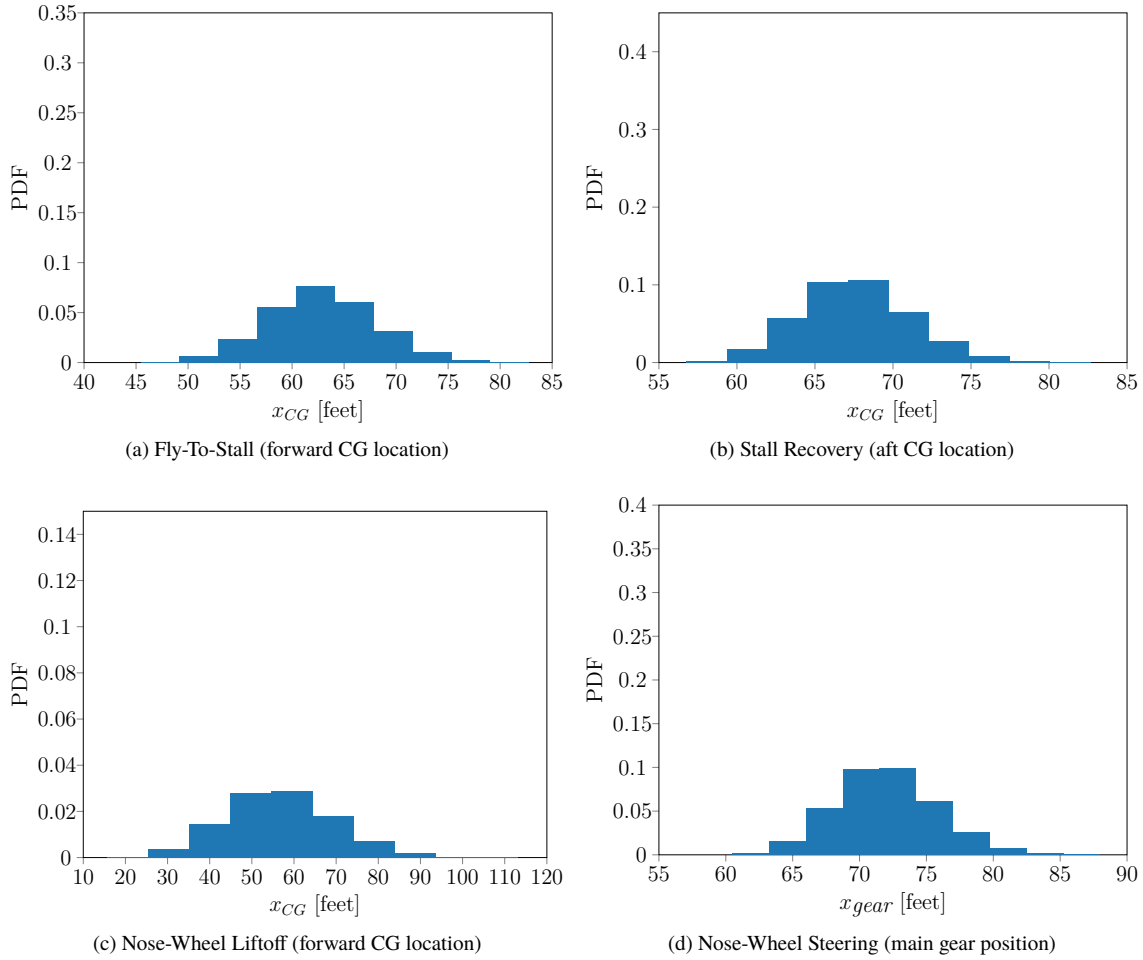


Fig. 18 Probability density histograms of each S&C criteria as estimated using 10,000 samples of the AVL aerodynamic data. All distances are given in feet.

over-speed on takeoff. This could allow the CG range to increase by relaxing the Nose-Wheel Lifftoff criterion constraints, thereby making it a non-critical forward limit criterion and allowing the S&C analysis to close. However this can only be done if the uncertainty in the Nose-Wheel Lifftoff range can be overcome through over-speeding on takeoff, which is not guaranteed. Allowing the aircraft to over-speed impacts the field length constraint analysis, as over-speeding increases the landing and takeoff field lengths. This in turn impacts braking, weight, and other performance requirements which the aircraft must meet. Thus, a balance must be struck between allowing for some uncertainty in the analysis of Nose-Wheel Lifftoff and the design of the rest of the system.

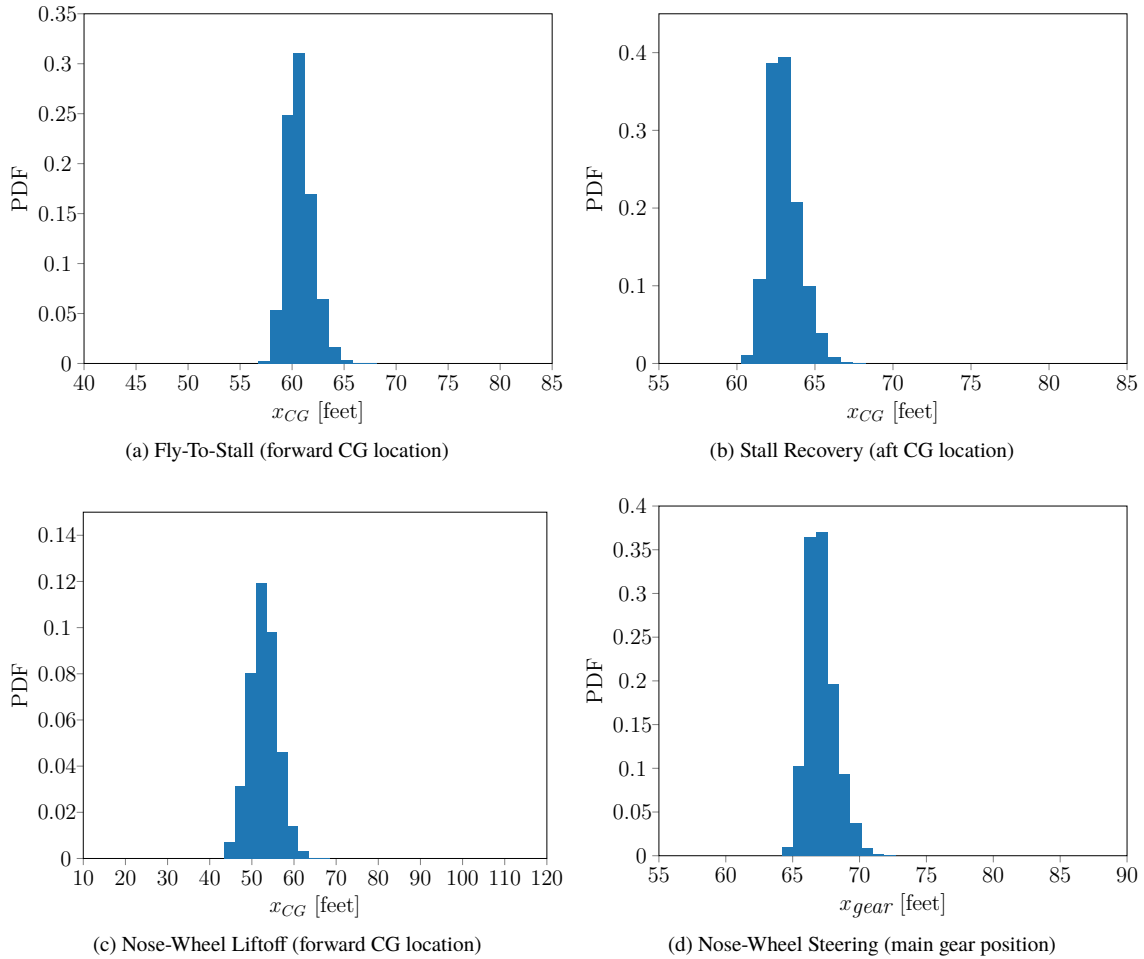


Fig. 19 Probability density histograms of each S&C criteria as predicted using 10,000 samples of the multifidelity aerodynamic data. All distances are given in feet.

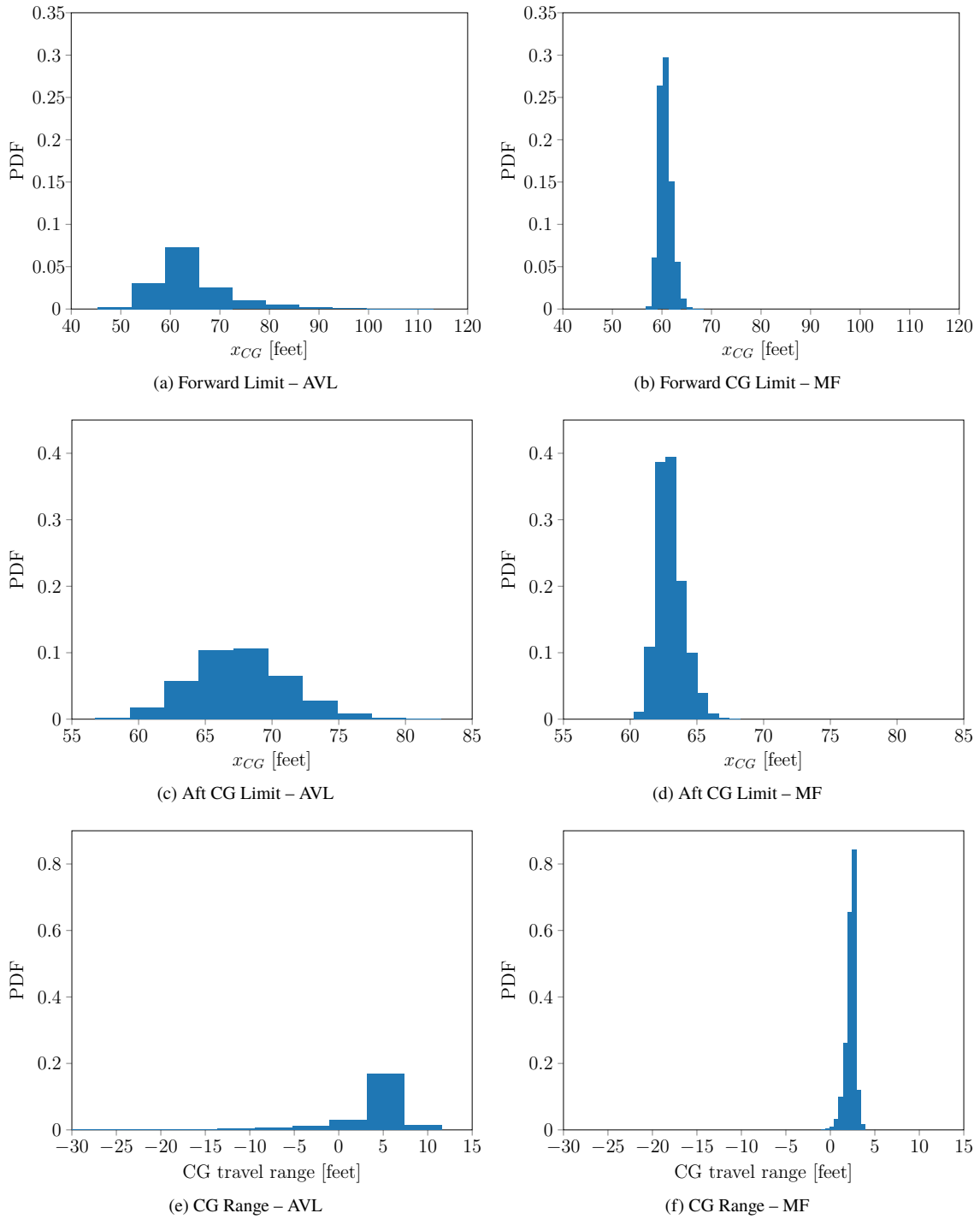


Fig. 20 Histograms of the forward and aft CG limits as well as the resulting CG range as computed using only the AVL data (left) and with the multifidelity (MF) models (right).

V. Conclusion

The work presented in this paper has shown the ability of a multifidelity methodology to bring high-fidelity data into an engineering analysis to reduce uncertainty in the output quantities of interest. By using all of the data available from all possible sources, even if for only a few points in a small segment of the analysis space, better decisions can be made due to the increased confidence in the predictive power of a multifidelity model as compared to a single-fidelity data source. Where more data are available for a given quantity of interest, uncertainty in the estimates of its value can be reduced, thereby reducing magnitude of the variances propagated to downstream quantities of interest. The BWB example illustrates this effect. When using only low-fidelity data, as is customary in a conceptual design phase, the estimates made regarding the CG limits and main gear location have a larger variance and in some cases a much different distribution than those estimated using the multifidelity models. While this paper illustrates the power of the multifidelity approach for an aircraft conceptual design problem, the methodology is broadly applicable and addresses challenges that arise more generally in design of multidisciplinary engineering systems.

Acknowledgments

This work was funded by The Boeing Company.

References

- [1] Liebeck, R. H., "Design of the Blended Wing Body Subsonic Transport," *Journal of Aircraft*, Vol. 41, No. 1, 2004, pp. 10–25. doi:10.2514/1.9084.
- [2] Cameron, D., and Princen, N., "Control allocation challenges and requirements for the Blended Wing Body," *AIAA-2000-4539, AIAA Guidance, Navigation, and Control Conference and Exhibit*, American Institute of Aeronautics and Astronautics, 2000. doi:10.2514/6.2000-4539.
- [3] Denieul, Y., Bordeneuve, J., Alazard, D., Toussaint, C., and Taquin, G., "Multicontrol Surface Optimization for Blended Wing-Body Under Handling Quality Constraints," *Journal of Aircraft*, Vol. 55, No. 2, 2018, pp. 638–651. doi:10.2514/1.C034268.
- [4] Garmendia, D. C., and Mavris, D. N., "Alternative Trim Analysis Formulations for Vehicles with Redundant Multi-Axis Control Surfaces," *Journal of Aircraft*, Vol. 53, No. 1, 2016, pp. 60–72. doi:10.2514/1.C033184.
- [5] Forrester, A., Sóbester, A., and Keane, A., "Multi-fidelity optimization via surrogate modelling," *Proceedings of the Royal Society of London A: Mathematical, Physical and Engineering Sciences*, Vol. 463, No. 2088, 2007, pp. 3251–3269. doi:10.1098/rspa.2007.1900.
- [6] Peherstorfer, B., Willcox, K., and Gunzburger, M., "Survey of multifidelity methods in uncertainty propagation, inference, and optimization," *SIAM Review*, Vol. 60, No. 3, 2018. doi:10.1137/16M1082469.
- [7] Alexandrov, N. M., Dennis, J. E., Lewis, R. M., and Torczon, V., "A trust-region framework for managing the use of approximation models in optimization," *Structural Optimization*, Vol. 15, No. 1, 1998, pp. 16–23. doi:10.1007/BF01197433.
- [8] Alexandrov, N., Lewis, R., Gumbert, C., Green, L., and Newman, P., "Approximation and Model Management in Aerodynamic Optimization with Variable-Fidelity Models," *Journal of Aircraft*, Vol. 38, No. 6, 2001, pp. 1093–1101. doi:10.2514/2.2877.
- [9] Eldred, M., Giunta, A., and Collis, S., "Second-Order Corrections for Surrogate-Based Optimization with Model Hierarchies," *AIAA-2004-4457, 10th AIAA/ISSMO Multidisciplinary Analysis and Optimization Conference*, American Institute of Aeronautics and Astronautics, 2004. doi:10.2514/6.2004-4457.
- [10] Keane, A. J., "Wing Optimization Using Design of Experiment, Response Surface, and Data Fusion Methods," *Journal of Aircraft*, Vol. 40, No. 4, 2003, pp. 741–750. doi:10.2514/2.3153.
- [11] Leary, S. J., Bhaskar, A., and Keane, A. J., "A knowledge-based approach to response surface modelling in multifidelity optimization," *Journal of Global Optimization*, Vol. 26, No. 3, 2003, pp. 297–319. doi:10.1023/A:1023283917997.
- [12] Poloczek, M., Wang, J., and Frazier, P. I., "Multi-Information Source Optimization," *Advances in Neural Information Processing Systems 30*, edited by I. Guyon, U. V. Luxburg, S. Bengio, H. Wallach, R. Fergus, S. Vishwanathan, and R. Garnett, Curran Associates, Inc., 2017, pp. 4288–4298.

- [13] Fischer, C., Grandhi, R., and Beran, P., “Bayesian low-fidelity correction approach to multi-fidelity aerospace design,” *58th AIAA/ASCE/AHS/ASC Structures, Structural Dynamics, and Materials Conference, AIAA-2017-0133*, 2017. doi:10.2514/6.2017-0133.
- [14] Balabanov, V., Grossman, B., Watson, L., Mason, W., and Haftka, R., “Multifidelity response surface model for HSCT wing bending material weight,” *7th AIAA/USAF/NASA/ISSMO Symposium on Multidisciplinary Analysis and Optimization, AIAA-98-4804*, 1998. doi:10.2514/6.1998-4804.
- [15] Choi, S., Alonso, J. J., Kroo, I. M., and Wintzer, M., “Multifidelity Design Optimization of Low-Boom Supersonic Jets,” *Journal of Aircraft*, Vol. 45, No. 1, 2008, pp. 106–118. doi:10.2514/1.28948.
- [16] Choi, S., Alonso, J. J., and Kroo, I. M., “Two-Level Multifidelity Design Optimization Studies for Supersonic Jets,” *Journal of Aircraft*, Vol. 46, No. 3, 2009, pp. 776–790. doi:10.2514/1.34362.
- [17] Wendorff, A. D., Alonso, J. J., and Bieniawski, S. R., “A Multi-Fidelity Approach to Quantification of Uncertainty in Stability and Control Databases for use in Stochastic Aircraft Simulations,” *16th AIAA/ISSMO Multidisciplinary Analysis and Optimization Conference*, American Institute of Aeronautics and Astronautics, Reston, Virginia, 2015, pp. 1–20. doi:10.2514/6.2015-3439.
- [18] Meyers, D. E., “Matrix Formulation of Co-Kriging,” *Mathematical Geology*, Vol. 14, No. 3, 1982, pp. 249–257. doi:10.1007/BF01032887.
- [19] Chung, H. S., and Alonso, J., “Design of a Low-Boom Supersonic Business Jet Using Cokriging Approximation Models,” *9th AIAA/ISSMO Symposium on Multidisciplinary Analysis and Optimization*, American Institute of Aeronautics and Astronautics, 2002. doi:10.2514/6.2002-5598.
- [20] Kuya, Y., Takeda, K., Zhang, X., and Forrester, A. I. J., “Multifidelity Surrogate Modeling of Experimental and Computational Aerodynamic Data Sets,” *AIAA Journal*, Vol. 49, No. 2, 2011, pp. 289–298. doi:10.2514/1.J050384.
- [21] Allaire, D., and Willcox, K., “A Mathematical and Computational Framework for Multifidelity Design and Analysis with Computer Models,” *International Journal for Uncertainty Quantification*, Vol. 4, No. 1, 2014, pp. 1–20. doi:10.1615/Int.J.UncertaintyQuantification.2013004121.
- [22] Lam, R., Allaire, D. L., and Willcox, K. E., “Multifidelity Optimization using Statistical Surrogate Modeling for Non-Hierarchical Information Sources,” *56th AIAA/ASCE/AHS/ASC Structures, Structural Dynamics, and Materials Conference*, American Institute of Aeronautics and Astronautics, 2015. doi:10.2514/6.2015-0143.
- [23] Ghoreishi, S. F., and Allaire, D. L., “A fusion-based multi-information source optimization approach using knowledge gradient policies,” *AIAA-2018-1159, 2018 AIAA/ASCE/AHS/ASC Structures, Structural Dynamics, and Materials Conference*, 2018. doi:10.2514/6.2018-1159.
- [24] Rasmussen, C. E., and Williams, C. K. I., *Gaussian Processes for Machine Learning*, The MIT Press, 2006. doi:10.7551/mitpress/3206.003.0001.
- [25] Forrester, A. I., Sobester, A., and Keane, A. J., *Engineering Design via Surrogate Modelling: A Practical Guide*, American Institute of Aeronautics and Astronautics, Reston, Virginia, 2008. doi:10.1002/9780470770801.
- [26] Winkler, R., “Combining Probability Distributions from Dependent Information Sources,” *Management Science*, Vol. 27, No. 4, 1981, pp. 479–488. doi:10.1287/mnsc.27.4.479.
- [27] Thomison, W., and Allaire, D., “A Model Reification Approach to Fusing Information from Multifidelity Information Sources,” *19th AIAA Non-Deterministic Approaches Conference, AIAA-2017-1949*, 2017. doi:10.2514/6.2017-1949.
- [28] Jaynes, E., “Information Theory and Statistical Mechanics,” *The Physical Review*, Vol. 106, No. 4, 1957, pp. 620–630. doi:10.1103/PhysRev.106.620.
- [29] Ayyub, B. M., and Klir, G. J., *Uncertainty Modeling and Analysis in Engineering and the Sciences*, Chapman and Hall/CRC, 2006. doi:10.1201/9781420011456.
- [30] Bae, H.-R., Grandhi, R. V., and Canfield, R. A., “An approximation approach for uncertainty quantification using evidence theory,” *Reliability Engineering & System Safety*, Vol. 86, No. 3, 2004, pp. 215–225. doi:10.1016/j.res.2004.01.011.
- [31] Zadeh, L. A., “Fuzzy sets,” *Information and Control*, Vol. 8, No. 3, 1965, pp. 338–353. doi:10.1016/S0019-9958(65)90241-X.
- [32] Rao, S. S., and Berke, L., “Analysis of uncertain structural systems using interval analysis,” *AIAA Journal*, Vol. 35, No. 4, 1997, pp. 727–735. doi:10.2514/2.164.

- [33] Liebeck, R., Page, M., and Rawdon, B., "Blended-wing-body subsonic commercial transport," *AIAA-1998-438, 36th AIAA Aerospace Sciences Meeting and Exhibit*, American Institute of Aeronautics and Astronautics, 1998. doi:10.2514/6.1998-438.
- [34] Haimes, R., and Dannenhoffer, J., "The Engineering Sketch Pad: A Solid-Modeling, Feature-Based, Web-Enabled System for Building Parametric Geometry," *AIAA-2013-3073, 21st AIAA Computational Fluid Dynamics Conference*, American Institute of Aeronautics and Astronautics, 2013. doi:10.2514/6.2013-3073.
- [35] Quinlan, J., and Gern, F. H., "Conceptual Design and Structural Optimization of NASA Environmentally Responsible Aviation (ERA) Hybrid Wing Body Aircraft," *57th AIAA/ASCE/AHS/ASC Structures, Structural Dynamics, and Materials Conference*, American Institute of Aeronautics and Astronautics, 2016, pp. 1–16. doi:10.2514/6.2016-0229.
- [36] Palacios, F., Alonso, J., Duraisamy, K., Colonno, M., Hicken, J., Aranake, A., Campos, A., Copeland, S., Economon, T., Lonkar, A., Lukaczyk, T., and Taylor, T., "Stanford University Unstructured (SU2): An open-source integrated computational environment for multi-physics simulation and design," *51st AIAA Aerospace Sciences Meeting including the New Horizons Forum and Aerospace Exposition*, American Institute of Aeronautics and Astronautics, 2013. doi:10.2514/6.2013-287.
- [37] Durham, W., *Aircraft Flight Dynamics and Control*, John Wiley & Sons, Ltd, 2013.
- [38] Filippone, A., *Advanced Aircraft Flight Performance*, Cambridge University Press, 2012. doi:10.1017/CBO9781139161893.
- [39] Schuler, J. M., and Dahl, M. A., "Proposed Revisions to MIL-F-8785C Related to Flight Safety of Augmented Aircraft," Tech. rep., Air Force Wright Aeronautical Laboratories, 1982.
- [40] Currey, N. S., *Aircraft Landing Gear Design: Principles and Practices*, American Institute of Aeronautics and Astronautics, 1988. doi:10.2514/4.861468.
- [41] McKay, M. D., Beckman, R. J., and Conover, W. J., "A Comparison of Three Methods for Selecting Values of Input Variables in the Analysis of Output from a Computer Code," *Technometrics*, Vol. 21, No. 2, 1979, pp. 239–245. doi:10.2307/1268522.